ARF-family global interactome mapping uncovers spatial organization of cellular signaling pathways

Laura Quirion[1,2], Amélie Robert[1], Jonathan Boulais[1], Shiying Huang[3], Yacine Kherdjemil[1], Denis Faubert[1], Marie-Pier Thibault[1], Marie Kmita[1,2,4,5], Jeremy M. Baskin[3], Anne-Claude Gingras[6,7], Matthew J. Smith[8] and Jean-François Côté[1,2,4,9,*]

[1]Montreal Clinical Research Institute (IRCM), Montréal, QC, H2W 1R7, Canada.

[2]Molecular Biology Programs, Université de Montréal, Montréal, QC, H3T 1J4, Canada.

[3]Department of Chemistry and Chemical Biology and Weill Institute for Cell and Molecular Biology, Cornell University, Ithaca, NY, 14853, USA.

[4]Department of Medicine, Université de Montréal, Montréal, QC, H3C 3J7, Canada.

[5]Department of Experimental Medicine, McGill University, Montréal, QC, H3G 2M1, Canada.

[6]Lunenfeld-Tanenbaum Research Institute, Sinai Health System, Toronto, ON, M5G 1X5, Canada.

[7]Department of Molecular Genetics, University of Toronto, Toronto, ON, M5S 1A8, Canada.

[8]Institute for Research in Immunology and Cancer, Université de Montréal, Montréal, QC, H3T 1J4, Canada.

[9]Department of Anatomy and Cell Biology, McGill University, Montréal, QC, H3A 0C7, Canada.

[*]Corresponding author:

Jean-François Côté, Ph.D.

110 pine avenue west

Montreal (QC) Canada

H2W1R7

E-mail: jean-francois.cote@ircm.qc.ca

ABSTRACT

The ADP-ribosylation factor (ARF) family of GTPases are essential molecular switches that control a large variety of cellular processes. Here, we used classical proximity-dependent biotin identification (BioID) to comprehensively define the interactome of 28 out of 29 ARF proteins in two cell lines. The identification of ~3000 high-confidence interactors allowed us to assign specific subcellular localization to the family members, uncovering previously undefined localization for ARL4D and ARL10. Clusterization analysis further showed the uniqueness in the set of interactors identified with these two ARF GTPases. We found that the expression of the understudied member ARL14 is restricted to the stomach and intestines and have identified phospholipase D1 (PLD1) and the ESCPE-1 complex, more precisely SNX1, as effectors. We showed that ARL14 can activate PLD1 *in cellulo* and is involved in the trafficking of cargos *via* the ESCPE-1 complex. Thus, the BioID data generated in this study represent a useful tool to dissect the intricacies of ARF signaling and its spatial organization.

INTRODUCTION

The ADP-ribosylation factor (ARF) family of small GTPases is part of the RAS superfamily together with RHO, RAS, RAN and RAB proteins. ARFs are involved in a plethora of cellular processes including bidirectional membrane trafficking, shaping membrane lipid composition, and dynamically remodeling the cytoskeleton (Sztul et al., 2019). As GTPases, they are presumed to cycle between an inactive GDP-bound conformation and an active GTP-bound conformation. This process is orchestrated by guanine nucleotide exchange factors (GEFs) through promotion of GDP dissociation allowing GTP binding, and GTPase activating proteins (GAPs) that augment intrinsic GTP hydrolysis (Bourne et al., 1991; Sztul et al., 2019). While other RAS proteins are lipidated at the C-terminus, the evolutionary conserved ARF family distinguishes itself by having a N-terminal extension, which forms an amphipathic helix in several members, that is modified with various lipid groups (Gillingham and Munro, 2007). This helix plays key regulatory functions, being buried in a hydrophobic pocket in inactive ARFs and becoming exposed and deeply inserted into membranes following GTP loading (Amor et al., 1994; Antonny et al., 1997). This unique feature positions ARF GTPases more proximal to membranes (1-2 nm) in contrast to other RAS-family proteins creating a unique signaling environment (Gillingham and Munro, 2007). Since ARFs coupling to effectors occur on membranes of complex lipid compositions and of various shapes, from flat to highly curved, and due to the difficulty to capture these events biochemically our current view of ARFs signaling is fragmented (Sztul et al., 2019).

The ARF family is composed of 29 members: 5 classical ARFs (Class I: ARF1, ARF3; Class II: ARF4, ARF5; and Class III: ARF6); 2 secretion-associated RAS (Nachury et al., 2007), 21 ARF-likes (ARLs), and the tripartite motif-containing protein 23 (TRIM23) (Gillingham and Munro, 2007). Classical ARFs are best characterized for recruiting coat proteins that initiate

vesicle formation for membrane trafficking and cargo transport (Tan and Gleeson, 2019). For example, ARF1, the founding member of the family, recruits the Coat Protein Complex I (COPI) at the Golgi membrane for retrograde vesicular transport of cargos to the endoplasmic reticulum (ER) (Palmer et al., 1993). ARF1 also orchestrates the formation of clathrin-coated vesicles at the Golgi by recruiting the adaptor-proteins AP-1/3/4 (Dittie et al., 1996; Hirst et al., 1999; Ooi et al., 1998) and GGA (Puertollano et al., 2001) proteins for vesicular trafficking to endosomes or plasma membrane. The unique functions of ARF3 and of ARF4/5 have been challenging to reveal since individual knockdowns do not induce a major detectable phenotype in cultured cells, but their co-depletion with ARF1 uncovered specific Golgi functions, suggesting that they support ARF1 functions in the secretory pathway (Volpicelli-Daley et al., 2005). Such data highlights a high degree of interplay in ARF-regulated pathways. Despite homology to ARF1, ARF6 predominantly acts at the cell periphery where it regulates endocytosis, endosomal recycling and the cytoskeleton, mainly via modification of membrane lipid compositions through activation of PI(4,5)-kinase (Honda et al., 1999), and phospholipase D1 (PLD1) (Toda et al., 1999), and *via* effects on actin by the activation of RHOA and RAC1 (D'Souza-Schorey and Chavrier, 2006; Santy et al., 2005). Similar to ARF1, SAR1A/B play conserved roles in ER-to-Golgi anterograde transport by recruiting the Coat Protein Complex II (COPII) and generating budding of vesicles (Jones et al., 2003; Saito et al., 2017). As paralogues, SARs have both overlapping and unique functions that can be attributed to differences in enzymatic and effector binding activity. For example, SAR1B distinguishes itself by having a slower GTP exchange activity and a higher affinity to SEC23 (Melville et al., 2020).

ARL proteins were discovered through sequence homology with ARF GTPases but are poorly studied in comparison to classical ARFs and SARs. ARLs control disparate biological

functions from diverse cell compartments (Kahn et al., 2006). Notably, ARL8A and ARL8B localize to lysosomes and promote their motility (Hofmann and Munro, 2006). Several ARLs (*e.g.*, ARL2/3, ARL4D, ARL6, ARL13B) regulate microtubule-associated processes at centrosomes, spindles, midbodies, basal bodies and cilia (Bhattarai et al., 2019; Li et al., 2010; Lin et al., 2020; Nachury et al., 2007; Yong et al., 2020; Zhou et al., 2006). The heterogeneous spatial distribution of some ARL proteins can drive interplay with multiple cellular processes. For example, ARL2 interacts with β-Tubulin and the Tubulin chaperone TBCD to promote cytosolic biogenesis of α/β-Tubulin dimers (Francis et al., 2017a; Francis et al., 2017b), and also localizes to the intermembrane space of mitochondria to drive mitochondrial fusion (Newman et al., 2017). The biological function of individual ARL GTPases is also complexified by interplay with other ARF family members. ARL1 crosstalk with ARF1/3 impacts recruitment of the GEF BIG1 at sorting endosomes (D'Souza et al., 2014), while ARL13B acts as a GEF for ARL3 to orchestrate the delivery of cargos into the cilium in cooperation with the ARF GAP RP2 (Gotthardt et al., 2015; Veltel et al., 2008). Globally, there are few known effectors of ARLs but these data are crucial to understand their cellular functions (Sztul et al., 2019). Indeed, little to no biological role have been attributed to ARL5C, ARL9, ARL10, ARL11, ARL13A, ARL14 or ARL16. Clearly, new approaches are needed to access unexplored layers of ARF spatial signaling and the full repertoire of associated proteins in cells.

Defective ARF signaling plays a role in numerous human diseases. Many genetic diseases are linked to mutations in coat complexes and are compiled as “Coatopathies”. These include mutations in COPI (DiStasio et al., 2017; Izumi et al., 2016; Watkin et al., 2015), AP (Abou Jamra et al., 2011; Assoum et al., 2016; Montpetit et al., 2008; Nesbit et al., 2013; Slabicki et al., 2010), COPII proteins (Bianchi et al., 2009; Boyadjiev et al., 2006; Garbes et al., 2015) and

Retromer (Damseh et al., 2015; Gustavsson et al., 2015). Mutations in ARF GEFs involved in coat assembly (Sheen et al., 2004) were also identified. In cancer, disruption of ARF-controlled membrane trafficking promotes cell invasion and migration (Casalou et al., 2020), and abnormal effector signaling can amplify oncogenic signals, such as ARF5/6-driven activation of PI3K/AKT (Nacke et al., 2021). ARFs are also hijacked by pathogens, including bacteria that directly subvert ARFs or their cognate effectors (Jimenez et al., 2016). Recently, ARF6 was described as an important host factor for the cell entry of the SARS-CoV-2 (Mirabelli et al., 2022; Zhou et al., 2022).

To gain fundamental knowledge into ARF signaling pathways and their relevance to cell biology and human health, we performed proximity labeling (BioID) coupled to mass spectrometry for 28 constitutively active human ARFs to define the global ARFome. Our approach reveals the broad landscape of ARF effectors and defines specificity for ARF GAPs. A complementary study investigated the proximity interactor of ARF proteins by short-term biotin labeling *via* miniTurboID (Li et al., 2022). Because BioID provides a 24-hour history of protein interactions, we could interrogate the localization of candidate proteins to define ARF localization and function at high resolution. Finally, we discovered a potential coat complex recruited *via* the newly identified PLD1 activator ARL14 on endosomes for retrograde traffic.

RESULTS

Using BioID to systematically define the ARF proximity interaction network

ARF GTPases are dynamic proteins that rely on a unique N-terminal region to insert in membranes to execute their functions. Therefore, a microenvironment more proximal to membranes, in comparison to other RAS and RHO proteins, is an integral part of ARF signaling. We predict that it will be challenging to capture many ARF-mediated interactions *in vitro* using classical biochemical approaches outside of this hydrophobic microenvironment. To circumvent this, we use BioID which proved a powerful method to systematically study RHO GTPases in their native environment (Bagci et al., 2020). The strength of BioID relies on an abortive biotin ligase derived from *Escherichia coli* that, when fused to a protein of interest, labels proximal interactors with biotin within a 10 nm radius (Roux et al., 2012). Irreversibly biotin-tagged proteins are affinity-purified with streptavidin and identified by mass spectrometry at high throughput (Nahle et al., 2022).

We systematically performed BioID following 24 hours of labeling time with 28 out of 29 ARF proteins as baits. TRIM23 was not included in the study due to unsuccessful cell line generation. BirA*-tagged GTPases were kept in a constitutively active state by mutation of glutamine in the highly conserved G-3 motif (WDXGG**Q**) that prevents hydrolysis of GTP. For ARF GTPases where this glutamine is not conserved, we generated the following mutants according to where the glutamine would fall: ARL5C (P70L), ARL9 (S151L), ARL10 (S132L), ARL13A (D75L), ARL15 (A86L), and SAR1A and B (H79G). ARL16 was kept in its wild-type form since the G-3 motif involved in GTP hydrolysis is atypical (RELGGC) (Dewees et al., 2022); the biochemical properties of ARL16 are unknown at this time. We elected to insert the BirA* tag at the C-terminal end of ARF proteins to leave unmodified the lipidated N-terminal extension, essential for membrane insertion (Fig 1A). With this approach,

we anticipated the enrichment of effectors and GAPs in the BioID screens, as we demonstrated for RHO proteins (Bagci et al., 2020). BirA*-Flag and BirA*-Flag-eGFP were used as controls to filter proteins randomly labeled with biotin. Likewise, BirA*-Flag-eGFP-CAAX was used as a control targeted to membranes to generate a ratio for filtering out proteins randomly labeled on membranes (see methods). All baits used in this study, and their mutations, are presented in Supplementary Table 1. To maximize the coverage and confidence in our proximity interactomes, we conducted BioID in two cell lines: Flp-In T-Rex HEK293 and Flp-In T-Rex HeLa. HEK293 cells have been a classical model for proteomics and HeLa cells for their oncogenic profile and for convenience of imaging. An advantage of using inducible cell lines is the ability to limit the long-term harm that the expression of the proteins of interest could cause to the cells. Upon generation of the cell lines, we validated the expression of all the baits, as well as their ability to biotinylate surrounding proteins by western blotting (Fig S1). We also analyzed the localization of all baits in cells by immunofluorescence (Fig S2), which revealed the well characterized classical ARFs to be localized as expected. We systematically conducted BioID screens for all baits and identified over 63,000 proximity interactions. Following stringent filtering (see Methods), 1265 high-confidence interactors in HEK293 cells and 1671 in HeLa cells were revealed, with 532 proximity interactors shared between the two cell lines (Fig 1A). The overlapping preys for each bait between the two cell lines, and the comparison with known interactions from the literature, are shown in Figure 1B. Overall, approximately 10% of our hits in HEK293 cells and 6% in HeLa cells overlap with the existing literature (Fig 1B) with the remainder representing novel interactions.

Previously known interactions were used to benchmark the quality of our BioID screens. Among the known binding partners, the ARF1 dataset contained GAPs (ARFGAP1, 2 and 3) and the COPI complex (α-, β-, γ-, δ- and ε-COP) required for retrograde trafficking from Golgi

to ER (Fig 1C). The complete COPII complex (SEC16A, SEC23A, SEC23B, SEC24B, SEC24C, SEC31A, SEC23IP and SEC13), required for anterograde trafficking between the same two compartments, was identified in the SAR1A dataset (Fig 1C). ARF6 BioID retrieved known interactors involved in modulation of lipid composition (PLD1, PIP5K) and endocytosis (AP2A1, AP2A2, AP2B1, AP2M1, CLTC, CLINT1, EPN2, PICALM, HIP1, HIP1R) (Fig 1C). The four metazoan GRIP domain golgins (GOLGA1, GOLGA4, GCC88 and GCC185) were identified using ARL1, which is required for their targeting to the Golgi (Panic et al., 2003; Setty et al., 2003) (Fig 1C). ARL2 was proximal to the TBCD and β-tubulin, that together form a trimer important for maintaining microtubule densities (Francis et al., 2017b) (Fig 1C). ARL15 functions as a negative regulator of cellular Mg^{2+} transport by modulating CNNMs N-glycosylation, and our BioID hits included three members of the Cyclin M family (CNNM2, CNNM3, CNNM4) and ribophorin I protein (RPN1) (Zolotarov et al., 2020) (Fig. 1C). The recall of these well-characterized interactions demonstrates the quality of the BioID screens and provides confidence in the potential of revealing new protein interactions and uncovering unsuspected functions for both the well-studied and understudied ARF proteins. The complete ARF BioID data are available for mining by the research community: http://prohits-web.lunenfeld.ca.

Mapping the distribution of ARF proteins *in cellulo* by their BioID

Precise localizations as well as detailed vesicular trafficking between intracellular compartments regulated by classical ARFs and atypical ARLs has been challenging to resolve using biochemical or epifluorescence microscopy. A strength of a classical BioID with 24 hours of labeling is the capture of a global picture of the transient protein interactions happening at specific subcellular locales during dynamic cellular processes like vesicular trafficking. Here, exploiting our BioID data, we aimed to assign to each bait their main intracellular localizations by querying the Human Cell Map database, a BioID-based online

tool that compared 192 subcellular markers to predict bait localization (Go et al., 2021). Using this, we systematically mapped the top 3 localizations of each ARF GTPase (Fig 2A). From our BioID, the tool identified at least one known localization predicted by literature searches for previously studied baits, except for ARFRP1, ARL4A and ARL11. Human Cell Map predicted a localization of ARFRP1 at the ER-Golgi intermediate compartment (ERGIC), peroxisome and nucleus, ARL4A at the ER and mitochondria and ARL11 at the ER and ERGIC. ARF1 served as a proof of concept as the results indicated a localization to the Golgi, notably with various Golgin family members as representative proximal proteins (GOLGA3, GOLGA5, GOLGB1) but also to the recycling endosomes with VPS50, part of the EARP complex as expected (Stearns et al., 1990),(Kondo et al., 2012). At some point during the 24 hours of incubation with biotin, SNARE proteins (VAMP3, VAMP8 and VTI1B) from the early endosome also became proximal to ARF1 (Fig 2A and B). With this method, new layers of information regarding the localization of previously known and unstudied ARF were identified.

ARL4D is an atypical GTPase which possesses in its C-terminus a short basic extension that functions as a nuclear localization signal (Jacobs et al., 1999) (Fig. S3A). BioID hits predicted a nuclear localization for ARL4D, but also comprised cytoplasmic proteins and surprisingly preys that localize to the nucleolus (Fig. 2A and B), though ARL4D staining itself was excluded from the nucleolar compartment (Fig. 2C). Co-staining of the biotinylated proteins with POP1, a nucleolus resident protein presenting high confidence proximity with ARL4D in HeLa cells (Fig 2B), confirmed the nucleolar enrichment of preys and suggests a role for ARL4D at the nucleoplasm-nucleolus interface (Fig 2C). No localization was previously assigned to the understudied ARF-family members ARL5C, ARL9 and ARL10. The BioID data suggest that ARL5C and ARL9 exercise their functions at the mitochondria as well as at both actin and

microtubule cytoskeleton (Fig 2A). Human cell map predicted that ARL10 accumulates at the mitochondria and in peroxisomes, as well as to the endoplasmic reticulum and nucleus at similar abundance (Fig 2A and B). Co-staining of ARL10 and the mitochondrial import receptor subunit TOM20 homolog (TOM20) confirmed a prominent mitochondrial localization of ARL10 (Fig 2D), independent of its GTP-loading state (Fig S3B). Moreover, high exposure of ARL10-GFP signal confirmed the presence of ARL10 in PEX14-positive peroxisomes (Fig 2D).

In contrast to most ARF family members, ARL10 lacks the classical N-terminal extension that is lipidated to favor membrane insertion. Instead, the classical ARF G-domain of ARL10 is preceded at the N-terminus by a 76 amino acid sequence without homology to any other members of the ARF family (Fig. S3A). To verify if this region contained a mitochondria-targeting signal, we created a chimera between the amino acids 1-76 of ARL10 and GFP ($ARL10^{1-76}$-GFP). The addition of $ARL10^{1-76}$ was sufficient to anchor GFP to the mitochondria, as shown with the colocalization with TOM20 (Fig. 2E and F). Analysis of ARL10 N-terminal sequence using membrane insertion prediction tool (TMHMM version 2.0) suggested the presence of a putative transmembrane (TM) domain spanning the amino acids 10-31. This region is mainly composed of hydrophobic residues and is followed by stretch of polybasic residues (PBR) as typically found in the N-terminus of signal-anchored mitochondrial outer membrane proteins (Fig S3A) (Walther and Rapaport, 2009). The deletion of the predicted transmembrane domain from the ARL10 sequence inhibited ARL10 mitochondrial localization ($ARL10^{\Delta 7-31}$, Fig 2E-F). However, the addition of ARL10 first 31 amino acids ($ARL10^{1-31}$) was not sufficient to induce the translocation of GFP to the mitochondria. Instead, $ARL10^{1-31}$-GFP was enriched in the Golgi apparatus as shown by the partial colocalization with the Golgi marker GM130 (Fig 2F). Altogether, these results

suggested the presence of a unique TM domain that functions with adjacent PBR for the efficient targeting of ARL10 to the outer membrane of the mitochondria.

Mapping the ARF effectors and regulators

One objective of performing BioID using constitutively active ARFs was to enrich effectors of these GTPases. To determine the specificity of effectors identified in individual datasets, we computationally generated an ARF-specificity score (ASS) and performed clusterization to underline the uniqueness of sets of preys to the baits (Fig 3A). The validity of this method is provided by the clusterization of baits with their closest relatives which have similar effectors. For example, classical ARFs except ARF6 clustered together, as did ARL5A and B, ARL8A and B and SAR1A and B. To further validate this method, we examined known unique interactions. For example, in the whole dataset the highest ASS was associated with TBCD in the BioID of ARL2 in HeLa cells, and the highest ASS score in the ARFRP1 dataset was for ARL3. Both are previously established interactions.

Clusterization analysis revealed many unique clusters, including Cluster 1 that is associated with SAR1B (Fig. 3B). It is known that SAR1B but not SAR1A mutations cause chylomicron retention disease, also known as Anderson disease, resulting in chylomicron secretion failure and fat malabsorption (Jones et al., 2003) (Shoulders et al., 2004). In addition to lipid malabsorption, SAR1B silencing in Caco-2/15 cells results in an increase of lipophagy while SAR1A silencing leads to the opposite phenotype (Sane et al., 2019). These previously identified functional differences between the two paralogs SAR1A and SAR1B are clearly reflected in their differential proximity interactomes. Some components of the COPII machinery were uniquely identified in the SAR1B dataset, including the SEC24D protein involved in cargo recognition, and MIA2 involved in large cargo secretion from the ER like chylomicron (Santos et al., 2016). Some preys also exclusively passed our stringent BioID

thresholding in SAR1B's interactome, namely BET1 a v-SNARE required for ER to Golgi transport (Mossessova et al., 2003) and TANGO1 (MIA3) involved in collagen secretion from the ER (Saito et al., 2011) (Raote et al., 2020). Furthermore, most of the proteins identified in Cluster 1 comprise a transmembrane domain and a few of them are involved in lipid metabolism (Fig. 3B). Together, these preys highlighted in the SAR1B dataset lays out research avenues to better understand the machinery and cargos of SAR1B-associated COPII vesicles.

Pathway enrichment analyses of individual clusters provide previously unknown localizations and functions for several ARFs. Cluster 5 is enriched in preys specifically identified with ARL4D, a GTPase known for its roles in actin remodeling (Li et al., 2007), neurite formation (Yamauchi et al., 2009), adipogenesis (Yu et al., 2011), microtubule growth (Lin et al., 2020), and immune functions (Geers et al., 2022) (Tolksdorf et al., 2018). Overrepresentation analyses of Gene ontology biological processes (GO BP) are consistent with ARL4D residency in the nucleus and potential functions in the nucleolus, but also reveals roles in ribosome biogenesis, regulation of RNA splicing, regulation of transcription, nucleosome organization, regulation of macromolecules biosynthetic process and RNA processing and modification (Fig. 3C). Cluster 2 and Cluster 3 were uniquely associated with ARL10 for which no biological function was previously identified. The enrichment analysis suggests a role for ARL10 in regulation of mitophagy, protein import into peroxisome, vacuolar transport, transport along microtubule, cilium organization, centrosome cycle and TOR signaling (Fig. 3D), consistent with its subcellular localization. To further delineate ARL10 functional role and obtain insights into its direct protein-protein interactions, an affinity purification-mass spectrometry (AP-MS) experiment was performed on ARL10 wild-type, constitutively active (S132L mutant) and nucleotide-free (S91N mutant) variants (Fig S4A). (Supplementary Table 6). The Gene Ontology analysis of biological processes showed an enrichment of mitochondrion

organization and transport, mitophagy and peroxisome organization with all variants. A set of biological processes were enriched with the nucleotide-free form, namely protein catabolic process, protein folding and protein insertion into mitochondrial outer membrane. The constitutively active mutant was enriched with processes revolving around phospholipid biosynthesis. Proteins complexed with wild-type ARL10 are involved in organelle localization, organic acid metabolic process, protein localization to peroxisome and TORC2 signaling (Fig S4A). The TORC2 signaling term was enriched in both the Cluster 3 (Fig. 3D) and the AP-MS results, with RICTOR and MAPKAP1, the core components of mTORC2 as its representatives. The AP-MS also retrieved all other accessory proteins associated with this complex except for DEPTOR and showed that ARL10 in its wild-type form is favorable for these interactions (Fig S4B). A co-immunoprecipitation confirmed the latter where ARL10 wild type has a stronger interaction with RICTOR than the constitutively active form. An interaction was not seen between RICTOR and the nucleotide-free form of ARL10 (Fig S4C).

Regulators of ARFs nucleotide cycling activity were also identified in our BioID datasets. The constitutively active GTPase mutants selected for proteomics were predicted to associate with GAP proteins specifically, being locked in GTP-loaded states, and we detected an abundance of GAPs but also GEF proteins in the datasets (Fig 4). Consistent with previous data, ARFGAP1, ARFGAP2 and ARFGAP3 were proximal to the classical ARF1/2/4/5. While ARFGAP2 and ARFGAP3 showed specificity, ARFGAP1 demonstrated promiscuity with several additional GTPases. AGFG1 was identified using class I classical ARFs (*i.e.* ARF1 and ARF3), class III (*i.e.* ARF6) as well as ARL8B and ARL13A. ARF6 was also in proximity of ACAP2, AGAP1 and AGAP3. In comparison to GAP regulators, the identified GEFs showed narrower specificity: ARFGEF2 was in the BioID of ARF1 and GBF1 was identified with ARL2. The GEF-like MON2 was identified with ARL1 and ARL10. In contrast, ARL13B is a

known GEF for ARL3 and was identified in numerous ARF GTPase datasets. Collectively, our data reveal many novel interactions between ARFs and candidate effectors, GEFs and GAPs, and future studies should aim to further understand their biological meaning.

The poorly characterized ARL14 is a robust PLD1 activator

Numerous members of the ARF family remained understudied, but ARL14 in particular is of interest due to role in cancer progression (Guo et al., 2019) (Zhang et al., 2021). According to single cell mRNA expression data deposited by the Human Protein Atlas, ARL14 expression is predicted in the gallbladder, stomach and intestines, and at a lower extent in the urinary bladder and pancreas (Uhlen et al., 2015) (proteinatlas.org). In the absence of suitable antibodies, we decided to validate the expression patterns of the ARL14 protein *in vivo* in mice by tagging ARL14 in its C-terminus with a 3xFlag epitope using the *i*-GONAD method (Gurumurthy et al., 2019). Mice were validated by sequencing the genomic locus and by using two genotyping strategies (Fig 5A and B). We isolated a panel of organs from adult wild-type or transgenic ARL14$^{+/3xFlag}$ mice, and western blotting analyses demonstrated that ARL14 is exclusively expressed in the stomach and in the small and large intestines (Fig 5C).

To study ARL14 signaling, we mined our BioID data in search of new partners that could act as effectors. Among the more prominent proteins in the ARL14 BioID was PLD1. Our data showed high spectral counts and the highest $\log_2$ fold change against the mean of the negative controls for PLD1 in both HEK293 and HeLa cells (Fig 5D). PLD1 hydrolyses phosphatidylcholine, an abundant phospholipid, into choline and phosphatidic acid (PA). PA is a cone-shaped signaling lipid that induces a negative curvature of membranes and also interacts with PA-binding proteins required for membrane fusion and fission (Zhukovsky et al., 2019) (Roth, 1999). ARF1 and ARF6 are among the classical activators of PLD1, and it is considered an effector of these GTPases (Hammond et al., 1995) (Frohman and Morris, 1999).

Though interactions of ARF1 and ARF6 with PLD1 were observed by BioID, the much higher PLD1 spectral counts obtained in the ARL14 BioID experiments suggest that ARL14 could be an important player involved in PLD1's activation (Fig 5E). Indeed, among the 28 ARFs tested we found only low spectral counts for PLD1 in the BioID studies of ARL4C, ARL8A and B, and ARL11, similar to those in the ARF1 and ARF6 experiments, suggesting a strong and specific interaction with ARL14. To validate this, we conducted a proximity ligation assay (PLA) in HeLa cells overexpressing ARL14-GFP and HA-PLD1 that confirmed PLD1 is proximal to ARL14 in its wild-type, nucleotide-free (S27N) and constitutively active (Q68L) forms with preference for the wild-type GTPase which showed the highest amount of PLA dots per cell (Fig 5F and G). To test whether ARL14 is able to activate PLD1, we used a click chemistry method termed IMPACT, for "Imaging PLD Activity with Clickable Alcohols *via* Transphosphatidylation" (Bumpus and Baskin, 2017) (Bumpus et al., 2020). IMPACT is a two-step procedure wherein (1) a clickable lipid is produced by PLD-mediated transphosphatidylation of phosphatidylcholine with an exogenous alcohol (3-azidopropanol) and (2) the clickable lipid produced is tagged with a fluorophore (BCN-BODIPY) by a click chemistry reaction. This experiment was performed on inducible HeLa cells overexpressing mScarlet, $ARF1^{WT}$-mScarlet, $ARL14^{WT}$-mScarlet or mutant variant of ARL14, and the fluorescent lipid product of the IMPACT labeling was measured by flow cytometry after thresholding on cells with similar mScarlet expression (Fig 5H). This *in cellulo* approach showed that ARL14 wild-type was the strongest PLD1 activator, with a 4.5-fold increase compared to the mScarlet control. The constitutively active ARL14 mutant showed a 3-fold increase in activity and ARF1 wild-type a 2-fold increase. The dominant negative ARL14 mutant was not able to activate PLD1, consistent with the requirement of an active GTPase to carry out a function. These data reveal ARL14 as a robust activator of its effector, PLD1.

ARL14 is involved in ESCPE-1 mediated trafficking

In addition to PLD1, the Endosomal SNX-BAR sorting complex for promoting exit-1 (ESCPE-1) complex, composed of dimers of SNX1 or SNX2 with SNX5 or SNX6, also emerged as a highly specific proximity interactor of ARL14 (Fig. 4D and 6A). SNX1 was among the preys with high spectral counts and high $\log_2$ fold change against the mean of the negative controls in both HEK293 and HeLa cells (Fig 5D). To investigate the role of nucleotide-loading of ARL14 for interaction with members of the ESCPE-1 complex, a PLA was performed on FlpIn T-Rex HeLa cells overexpressing ARL14-GFP wild-type, constitutively active (Q68L) or nucleotide-free (S27N) vairants. It showed that endogenous SNX1 is proximal to wild-type and constitutively active ARL14 but not to the nucleotide free mutant, suggesting that SNX1 is a classic effector binding to the GTP-loaded form of ARL14 (Fig 6B and C). Surprisingly, endogenous SNX6 remains proximal to ARL14 independently of its activation state (Fig S5A).

To establish a subcellular localization for the ARL14 and ESCPE-1 complex, FlpIn HeLa cells expressing ARL14-mScalet WT, Q68L or S27N were fixed and stained for SNX1 or SNX6. Since the SNX-BAR proteins are critical for both endosome-to-plasma membrane recycling and endosome-to-TGN retrieval, it was anticipated that ARL14 and SNX would colocalize in least in one of these locations. We observed that wild-type and constitutively active ARL14-mScarlet were partially soluble in the cytoplasm with some enrichment in puncta reminiscent of endosomes and at the plasma membrane, while ARL14-mScarlet in its nucleotide-free form was either soluble or in puncta (Fig. 6D and Fig. S5B). ARL14 WT- or Q68L-positive puncta are often juxtaposed with SNX1 or SNX6 puncta while ARL14 S27N-positive puncta showed only rare overlap with SNX1 and SNX6 staining (see enlargement Fig 6D and Fig. S5B). More strikingly, we observed accumulation of SNX1 or SNX6 puncta along ARL14 WT- or Q68L-

enriched domains of the plasma membrane. Altogether, these results suggested that ARL14 interacts with the ESCPE-1 complex.

In addition to its roles in phospholipid recognition and membrane tubulation, ESCPE-1 functions as a recognition and sorting module for a subset of transmembrane proteins transiting in the endosomes (Simonetti et al., 2019). The best characterized ESCPE-1 cargo is the Cation-Independent Mannose-6-Phosphate Receptor (CI-MPR) (Fig S5C). Previous studies showed that depletion of SNX5 and SNX6 inhibited CI-MPR retrieval from the endosome to the TGN, causing an accumulation of CI-MPR outside the TGN (Kvainickas et al., 2017) (Simonetti et al., 2017). To test whether ARL14 has a function in ESCPE-1 mediated trafficking, we generated ARL14 knock-out HeLa cells by CRISPR/Cas9. Unfortunately, we were unable to generate antibodies specific to ARL14, so we validated the efficiency of *ARL14* genomic deletion by sequencing genomic DNA (Fig S5G). We then measured the effect of ARL14 knock-out on CI-MPR localization. Our results showed that genetic inactivation of *ARL14* impairs CI-MPR retrieval to the TGN (Fig 6E and F). As a validation control, we also observed that siRNAs targeting SNX5 and SNX6 impaired CI-MPR retrieval to the TGN (Fig S5D-F). Collectively, these results support a previously unknown role for ARL14 in the regulation of the ESCPE-1 complex.

DISCUSSION

ARF GTPases are key regulators of a large array of cellular processes for which protein-protein interactions on membrane-rich compartments are essential. While classical ARFs are well-studied, the localization and functions of ARL proteins have been poorly defined. Here, we systematically delineated the proximity interactomes of all ARF family members, except TRIM23, using BioID, a powerful tool to identify stable or transient protein proximity interactions in their native environment. Our data drastically expand the repertoire of candidate interactors of ARFs and ARF-related proteins. These publicly deposited data can be mined by the research community to generate new hypotheses. In this study, we only began to extract new information from the large dataset, notably on the subcellular compartments on which each ARFs exerts its functions, its proximity interactors, and new functional data for the poorly studied ARL10 and ARL14 family-members.

There are some limitations to our approach, particularly that we must overexpress tagged proteins which could either create artifacts or hinder some interactions. Unfortunately, this is a necessity with small G-proteins that presumably only function in an activated state (GTP-bound). Nonetheless, it remains important to validate BioID interactions using additional methods. Here, we also restricted our analysis of ARFs to HEK293 and HeLa cells, undoubtedly missing specialized functions and additional interactors specific to different cell types (for example ARL14 seems to be mostly expressed in gastrointestinal cells). Furthermore, as it is not known how most ARF GTPases become endogenously activated, the BioID screen was performed on the constitutively active mutants. The activating mutations were designed using sequence homology to well characterized classical ARFs, but a caveat of working with understudied proteins is that we do not know if they will affect GTPase cycling as expected, and this is especially true given that some ARLs are known to have weaker affinity

for nucleotides than RAS and RHO (Jacobs et al., 1999) (Linari et al., 1999) (Hanzal-Bayer et al., 2005). The last statement is supported by the few known ARF GAPs that were identified in the BioID, particularly with ARLs. This suggests that alternative mechanisms of ARF GTPases regulation must exist in cells, including stabilization of GTP-binding in presence of an effector. In the future, dedicated efforts will be needed to characterize the biochemical activity of the atypical proteins such as ARL10 and ARL14 that we studied here by cell biology. As for the identification of GEFs, their presence in the BioID of constitutively active forms of ARF GTPases could indicate the existence of signaling cascades within the family where GEFs can be recruited as effectors of one ARF to regulate the activity of another ARF, as seen for RHO (Bagci et al., 2020) and RAS GTPases (Yoshikawa et al., 2007).

One of the main goals of this study was to attribute potential functions to the most uncharacterized ARF family members. The understudied ARL10 caught our attention as its BioID data revealed localization to mitochondria. We determined that this localization is mediated *via* a unique transmembrane domain followed by a polybasic region. Mitochondrial localization is independent of the nucleotide-loading state of the GTPase. The BioID and complementary AP-MS studies highlighted that ARL10 may regulate mitophagy, mitochondrial fission, and several metabolic processes. The association of ARL10 with the mTORC2 complex was also observed in both BioID and AP-MS, and was validated by co-immunoprecipitation with RICTOR. Given that ARL10 is localized at the mitochondria, this may provide insight on the function and regulation of the small active pool of mTORC2 previously observed at this location (Ebner et al., 2017). Furthermore, our ARL10 BioID data also identified several peroxisome-resident proteins. The presence of a small pool of ARL10 at peroxisomes was confirmed by co-immunostaining. Peroxisome and mitochondria are closely related organelles that communicate together through small vesicles (Neuspiel et al.,

2008). The identification of proteins involved in mitochondrial dynamics, *i.e.* fusion and fission, in the BioID as well as the validated localization of ARL10 to both these organelles imply that this GTPase might be involved in this communication process, which requires further validation. A recent study demonstrated that ARL10 is indeed detectable on vesicles derived from mitochondria (Konig et al., 2021).

While our study was under completion, Li *et al.* published an ARF GTPase interactome. They elected to use a miniTurboID approach, where biotin labeling was done for only 15 minutes, on 25 members of the family (excluding ARL4A, ARL5C, ARL9 and ARL13A). In contrast to our approach of expressing the baits in a tetracycline-inducible manner, they infected HEK293A cells for stable expression. We performed BioID on 28 members, excluding TRIM23, in inducible HEK293 and HeLa cells to have less toxicity or alterations in gene expression resulting from stable and uncontrolled overexpression of constitutively active GTPases. The Li *et al.* study and our work presented here are highly complementary. Notably, the short versus long-term labeling provides different information. Short labeling reveals the interactions that are most frequently occurring while a longer labeling strategy will also highlight transient interactions, increase the number of proximal interactors, and catch interactions dependent on specific cell states (*e.g.* during the cell cycle). We compared the Li *et al.* hits to our datasets obtained in HEK293 cells for the 24 common baits. We estimate that ~350 interactions are shared, which leaves ~1400 new proximity interactors identified by our BioID. A weakness of the Li *et al.* approach is the lower spectral counts observed (due to short labeling time) and as such, the correlation of their data among replicates is low (some of their correlation coefficients are as low as 0.4 while ours are all above 0.9) and no statistical data is provided. In contrast, we used non-specific baits (BirA*, BirA*-eGFP and BirA*-eGFP-CAAX) to filter noise from our ARF baits, and provide statistical confidence for all our data.

In conclusion we believe that together, these two studies present a major advance in obtaining an accurate representation of the whole ARF-family interactome.

Like us, Li *et al.* noted the robust interaction between PLD1 and ARL14. They showed that ARL14 is a PLD1 activator in an *in vitro* assay, while we used an *in cellulo* approach to show ARL14-mediated activation of PLD1, therefore supporting and strengthening this conclusion. The work here is also highly complementary. Li *et al.* mapped the essential region in PLD1 for ARL14-binding. Instead, we conducted functional studies that additionally identified the ESCPE-1 complex as a candidate effector of ARL14. Our work demonstrated that CI-MPR failed to be retrieved in the Golgi in ARL14-null HeLa cells. SNX1 was also identified in the miniTurboID of ARL14, reinforcing our hypothesis that SNX1 is an ARL14 effector. We note that SNX1, 2, 5 and 6 are also involved with the SNX-BAR Retromer complex composed of the VPS35–VPS26–VPS29 heterotrimer and a dimer of SNX1 or 2 with SNX5 or 6 (Bonifacino and Hurley, 2008). Though the VPS trimer was not identified in either of the proximity labeling approaches, it cannot be excluded at this time that ARL14 could also be involved in this complex. Further experiments will be required to discriminate the implication of ARL14 in both complexes. From the accumulated results, we suggest that the ESCPE-1 complex and PLD1 could work collaboratively to generate endosomes. Activated ARL14 could insert into endosomal membranes, causing a local positive curvature that attracts ESCPE-1 as coats, leading to tubulation and concentration of cargos. In parallel, the recruitment and activation of PLD1 by ARL14 to produce PA could enhance membrane curvature to generate those newly formed endosomes. Our work additionally reveals that ARL14 is restricted in expression in gastrointestinal cells of humans and mice. It will be interesting to fully characterize the role of ARL14, and the interactions with PLD1 and ESCPE-1, in specialized cells of the intestines where these new protein-protein interactions may be involved in important secretory functions.

Globally, our study demonstrated the potential of our dataset for the discovery of new ARF and ARF-like protein functions and modes of regulation. Our BioID data is available on the website to assist the research community in exploring the ARF interactions.

METHODS

Antibodies, plasmids, siRNAs, primers, cDNA and cloning

The antibodies used in this study are presented in Supplementary Table 2, plasmids in Supplementary Table 3, siRNAs in Supplementary Table 4 and primers in Supplementary Table 5. The NCBI Reference Sequence number of the complementary DNA (cDNA) of ARF proteins used in this study is listed in Supplementary Table 1. All coding sequences were synthesized as previously described (Patel et al., 2011) except ARL6, ARL9 and ARL16 for which sequences were retrieved with NCBI and synthetized with Gateway compatible AttB sites (Twist Bioscience). The Gateway cloning system (Invitrogen) was used to recombine the cDNA sequences in the entry vector (pDONR221). Every ARF cDNA were then recombined into the expression vector pcDNA5-pDEST-FRT-BirA*-Flag-CT (Couzens et al., 2013). The fluorescent destination vector pcDNA5-pDEST-FRT-eGFP-CT (Kean et al., 2011) was used for ARL10 and ARL14 and pcDNA5-pDEST-FRT-mScarlet-CT for ARL14. To create pcDNA5-pDEST-FRT-mScarlet-CT, mScarlet was amplified from pMaCTag-Z11 (Addgene# 120054) using KpnI/XhoI compatible primers and the resulting mScarlet cDNA was used to replace eGFP from pcDNA5-pDEST-FRT-eGFP-CT following digestion with KpnI and XhoI.

Cell culture and transfections

Flp-In™ T-Rex™ HEK293 (Thermo Fisher), Flp-In™ T-Rex™ HeLa (gift from S. Taylor, University of Manchester UK) and HeLa cell lines were maintained at 37 °C and 5% CO_2 and grown in Dulbecco's modified Eagle's medium (DMEM) supplemented with 10% fetal bovine serum (FBS) (F1051, Sigma-Aldrich) and 1% penicillin–streptomycin (P/S) (450-201-EL, Wisent). Stable cell lines were generated as previously described (Nahle et al., 2022) and were grown in DMEM supplemented with 10% tetracycline-free FBS (081-150, Wisent) and 1% P/S. To induce protein expression, stable cell lines were treated with 1 ug/mL of tetracycline with or without 50 µM biotin treatment. SiRNA transfections were performed using

Dharmafect-1 (GE Healthcare) and 80nM of indicated siRNA. DNA transfections were performed with Lipofectamine™ 3000 according to the manufacturer (L3000001, Thermo Fisher).

BioID and mass spectrometry injections

BioID experiments were performed as previously described (Bagci et al., 2020) and the extensive protocol for BioID and MS injection was further detailed (Nahle et al., 2022). Briefly, cells were lysed using RIPA lysis buffer [1% NP-40, 50mM Tris-HCl pH 7.4, 0.1% SDS, 150mM NaCl, 0.5% sodium deoxycholate, 1mM EDTA pH 8] and sonication was performed. Biotinylated proteins were retrieved from cleared lysates by incubation with 70 µl of streptavidin beads (17-5113-01, GE Healthcare) for 3h at 4°C. Following washes with lysis buffer and ammonium bicarbonate (AB0032, Biobasic), on-beads digestion was performed overnight with 1 ng/µL of trypsin (T6567, Sigma-Aldrich). An additional 2h incubation at a final concentration of 2 ng/µL of trypsin was done. Digested peptides were recovered, and beads were washed with water. Formic acid (94318, Sigma-Aldrich) was added to a final concentration of 5% to end tryptic digestion. Peptides were dried down in a SpeedVac, resuspended in 15 µl of 5% formic acid and stored at -80°C. HEK293 samples were analyzed with a LTQ-Orbitrap Velos (Thermo Fisher) and HeLa samples with a Q Exactive (Thermo Fisher). Samples were loaded into a 75 µm i.d. × 150 mm Self-Pack C18 column installed on the Easy-Easy-nLC 1000 system (Proxeon Biosystems). Peptides were eluted with a two-slope gradient at a flow rate of 250 nL/min, from 2% to 35% in 100 min and then from 35 to 80% in 10 min transferring from buffer A [0.2% formic acid] to buffer B [90% acetonitrile/0.2% formic acid]. Peptides were ionized using a Nanospray Flex Ion Source on both instruments. Acquisition in the Orbitrap was made with a full-scan MS survey scanning (m/z 360–2,000) in profile mode with a resolution of 60,000, an AGC target at 1E6 and a maximum ion time of 100 ms. Nanospray and S-lens voltages were set to 1.3–1.8 kV and 50 V, respectively. Capillary

temperature was set to 250ºC. On the LTQ Orbitrap Velos, the 11 most intense peptide ions were fragmented by collision-induced dissociation fragmentation and MS/MS spectra were acquired in the linear ion trap with an AGC target at 1E4 and a maximum ion time of 100 ms. MS/MS parameters were: normalized collision energy, 35 V; activation q, 0.25; activation time, 10 ms and target ions already selected for MS/MS were dynamically excluded for 30s. For the Q Exactive, the 16 most intense peptide ions were fragmented by higher-energy collisional fragmentation and MS/MS spectra were acquired in the Orbitrap with a resolution of 17,500, an AGC target at 1E5 and a maximum ion time of 50 ms. MS/MS parameters were: normalized collision energy at 27 and target ions already selected for MS/MS were dynamically excluded for 7s.

Mass spectrometry data analyses

Raw mass spectrometry files were analyzed by the X! Tandem (Craig and Beavis, 2004) and Mascot search engines through the iProphet pipeline (Shteynberg et al., 2011) integrated in Prohits (Liu et al., 2010). Searches were performed using the Human RefSeq protein sequence database (2017 version) supplemented with "common contaminants" from the Max Planck Institute (http://maxquant.org/downloads.htm), the Global Proteome Machine (GPM; http://www.thegpm.org/crap/index.html) and decoy sequences. The Mascot parameters were set with strict trypsin specificity (two missed cleavage sites allowed) and Oxidation (M) and Deamidation (NQ) as variable modifications. The mass tolerances for precursor and fragment ions were set to 10 ppm and 0.6 Da, respectively, and peptide charges of +2, +3 and +4 were considered. The resulting X! Tandem and Mascot search results were individually processed by PeptideProphet (Keller et al., 2002), and peptides were assembled into proteins using parsimony rules first described in ProteinProphet (Nesvizhskii et al., 2003) using the Trans-Proteomic Pipeline (TPP). TPP settings were the following: -p 0.05 -x20 -PPM –d“DECOY”, iprophet options: pPRIME and PeptideProphet: pP. Samples reproducibility among biological

replicates was assessed in R (r-project.org) by performing multidimensional scaling with the limma package (Ritchie et al, 2015) and Spearman correlations with the stats package using spectral counts of identified preys. We discarded and reacquired biological replicates displaying Spearman correlations lower than 0.9 and/or clustered poorly among biological replicates on a MDS plot.

Interactions scoring

To calculate statistics on the interactions, we used SAINTexpress (Teo et al., 2014) (version 3.6.1) on proteins with iProphet protein probability ≥ 0.9 and unique peptides ≥ 2. Proteomics datasets (ARFs BioID screens in HEK293 and HeLa cells) were compared separately against their respective negative controls. These controls comprised of pulldowns performed on both cell lines expressing either the eGFP-BirA*-Flag vector or the empty vector (devoid of the BirA*-Flag), each in biological duplicates. SAINT analyses were performed without control or bait compression. To infer ARFs' high confidence interacting proteins, we applied, in addition to the SAINT average probability (AvgP) ≥ 0.95 threshold (more stringent than a BFDR ≤ 0.01 threshold), a combination of two additional filters: the preys' Average Spectral count (AvgSpec) and the preys' CAAX ratio (Preys AvgSpec/CAAX AvgSpec). For each of the cell lines, the cutpoints of both additional filters were estimated by cumulative distribution (CDA) and ROC sensitivity analyses. After identifying ARFs physical recall interactions, as reported by the human BioGrid database (v 4.4.210) (Chatr-Aryamontri et al., 2017), we performed CDA and ROC sensitivity analysis in R with the mltools and cutpointr packages respectively. To gain precision, we limited these analyses to ARF1, ARF6, SAR1A and SAR1B, which have been, up to this date, the most characterized proteins of the ARF family. From the results of these approaches, we reasoned that AvgSpec thresholds of 4.5 and 6, with a CAAX ratio of 1.7, were the most appropriate for the HEK293 and HeLa datasets respectively. Unfiltered contaminants, such as Keratin, BirA*, carboxylases and beta

galactosidase were manually removed. To assess the specificity of each interaction among the ARFs interactome, we calculated for each cell line their WD-score by using the SMAD R package (Sowa et al., 2009). Next, we pooled the interactions specificity of both cell lines by summing their respective WD-scores, giving us a "Summed WD-Score" that we referred to as ASS score. The benefit of this metric is to increase our capacity to identify ARF interactors of high confidence, either from interactions shared by both cell lines or from unique cell line interactions. We then exploited this Summed WD-Score metric by building a heatmap of ARFs effectors with the R complexheatmap package (Gu et al., 2016). To do so, we selected potential ARFs effectors by removing ARFGAPs and ARFGEFs from filtered ARFs interactions. Then we calculated Canberra distances between filtered preys and Pearson correlations between baits, and used the Ward.D method to extract 16 clusters of preys and 13 clusters of baits. Similarly, heatmaps of ARFGAPs and ARFGEFs were also created without cluster extraction. For each of the clusters of ARFs effectors, we performed an over-representation analysis of GO BP in R using the gprofiler2 package (Kolberg et al., 2020). The complete lists of interactions with scores and annotations are available online at the following website: http://prohits-web.lunenfeld.ca.

Bioinfo and network analyses

Proportional area chart was created in R with the ggplot2 package. Analysis of each ARF subcellular localization was executed separately on the Cell Map website (cell-map.org) and filtered to the top three subcellular localizations with the shortest distances. Graphical representations of protein-protein networks were generated in Cytoscape (Shannon et al., 2003) (version 3.9.1). Illustration of the ARFs' subcellular localizations was inspired by the animal cell drawing from the SwissBioPics website (swissbiopics.org). Dotplot representations of interactions were generated at the ProHits-viz website (prohits-viz.org). Enrichment maps of GO BP were generated in Cytoscape with the EnrichmentMap app (v 3.3.4) (Merico et al.,

2010), by loading overrepresented GO BP estimated with fdr correction by gProfiler (Raudvere et al, 2019). CBN(P) normalized values were calculated as previously described (Cozzolino et al, 2020).

Immunofluorescence staining, imaging, and analyses

Cells were fixed with 3.7% formaldehyde in CSK buffer [100 mM NaCl, 300 mM sucrose, 3 mM $MgCl_2$, 10 mM PIPES, pH 6.8] for 15 min and permeabilized with 0.2% Triton X-100 in PBS for 5 min. Then, cells were incubated with primary antibody in the wash buffer [1% BSA, 0.1% Triton-X100 in TBS], washed with wash buffer and incubated for 30 min with the appropriate secondary antibody. Hoechst, phalloidin and/or streptavidin were incubated together with secondary antibodies when indicated. Cells were washed with the wash buffer and then once with water. Coverslips were mounted with Mowiol. Images were acquired with a Carl Zeiss LSM700 laser scanning confocal microscope (Carl Zeiss MicroImaging, Jena, Germany) equipped with a plan-apochromat ×63/1.4 numerical aperture objective and operated with ZenBlack 2009. Fiji (Schindelin et al., 2012) (v2.0.0-rc-69/1.52k) was used for analyses. CI-MPR fluorescence intensity was quantified by measuring CI-MPR mean intensity across the whole cell excluding the TGN.

Co-immunoprecipitation and affinity purification-mass spectrometry

For enrichment of ARL10 complex, FlpIn HeLa ARL10-GFP cells were lysed in digitonin buffer [50 mM HEPES pH 7.4, 120 mM NaCl, 0.5% digitonin, 0.25 mM $NaVO_3$, 1 mM PMSF, 10mM NaF] supplemented with EDTA-free Protease Inhibitor Cocktail (4693132001, Sigma-Aldrich). 1mg of cleared cells lysate was incubated with 10 µL of GFP-selector affinity resin developed by NanoTag Biotechnologies (N0310, Synaptic Systems) for 2h at 4°C. Beads were washed three times with lysis buffer, resuspended in 30 µl of Laemmli buffer [5% SDS, 0.1

mM Tris pH 6.8, 140 mM β-mercaptoethanol, 25% glycerol] and denatured for 5 min at 95°C for western blotting.

For affinity purification-mass spectrometry of the ARL10-GFP complex, the three washes of the pulled down GFP-selector beads with lysis buffer were followed by two additional washes with 50 mM HEPES/120 mM NaCl to remove detergents. Samples were then reduced with 9 mM dithiothreitol at 37ºC for 30 minutes and, after cooling for 5 minutes, alkylated with 17 mM iodoacetamide at room temperature for 30 minutes in the dark. Prior to protein digestion, a Protein Aggregation Capture using Hydroxyl beads (ReSyn Biosciences) was performed to remove SDS and glycerol. The proteins were digested on-beads with Trypsin (Promega) with ratio enzyme:proteins 1:20 in 50 mM ammonium bicarbonate and performed overnight at 37ºC. For each sample, the supernatant was transferred into a new sample tube and dried with a vacuum centrifuge (Eppendorf). Samples were reconstituted under agitation for 15 min in 11 µL of 2%ACN-1%FA and loaded into a 75 µm i.d. × 150 mm Self-Pack C18 column installed in the Easy-nLC II system (Proxeon Biosystems). Peptides were eluted with a two-slope gradient at a flow rate of 250 nL/min. Solvent B first increased from 2 to 35% in 120 min and then from 35 to 85% B in 20 min. The HPLC system was coupled to Orbitrap Fusion mass spectrometer (Thermo Scientific) through a Nanospray Flex Ion Source. Nanospray and S-lens voltages were set to 1.3-1.7 kV and 50 V, respectively. Capillary temperature was set to 225 °C. Full scan MS survey spectra (m/z 360-1560) in profile mode were acquired in the Orbitrap with a resolution of 120,000 with a target value at 1e6. The 25 most intense peptide ions were fragmented in the HCD collision cell and analyzed in the linear ion trap with a target value at 1e4 and a normalized collision energy at 29 V. Target ions selected for fragmentation were dynamically excluded for 20 sec after two MS2 events.

Animal experiments

Mice were housed in a specific pathogen-free (SPF) facility and experiments were approved by the Animal Care Committee of the Montreal Clinical Research Institute in compliance with the Canadian Council of Animal Care guidelines (protocols 2021-04 MK). ARL14^{3xFlag} knock-in alleles were generated by CRISPR/Cas9 mediated gene editing using *i*-GONAD procedure (Gurumurthy et al., 2019). Briefly, Cas9 ribonucloprotiens (RNPs) mix containing 6 µM Cas9 proteins (S.p. HiFi Cas9 Nuclease V3, 1081061, Integrated DNA Technologies) 30 µM gRNA and corresponding30 µM ssDNA mix were delivered by microcapillary injection into ampulla of 6 to 10 weeks old CD-1 pregnant females at 0.7 days post conception, followed by electroporation of the oviduct. Mice were genotyped by PCR followed by Sanger sequencing to verify correct targeting. We used Integrated DNA Technologies (IDT) tool to select gRNA (https://www.idtdna.com/site/order/designtool/index/CRISPR_CUSTOM). All sequences and reagents used are described in Supplementary Table 5.

For organ collection, male mice of 65 days of age were sacrificed and dissected. Organs were flash frozen and kept at -80°C. Organs were grinded in liquid nitrogen with an additional shredding step for muscles then lysed in RIPA lysis buffer supplemented with inhibitors as described above. Proteins were then quantified from cleared lysates and samples were run on SDS-page. The top half portion of the gel was used for Coomassie Brilliant Blue R-250 staining and the bottom half was used for immunoblotting.

Proximity ligation assay

Cells were fixed and permeabilized as described for immunofluorescence staining. PLA was performed using the Duolink® In Situ Detection Reagents Red (DUO92008, Sigma-Aldrich) with the anti-mouse MINUS (DUO92004, Sigma-Aldrich) and anti-rabbit PLUS (DUO92002, Sigma-Aldrich) probes. Images were acquired with a DM6 upright microscope (Leica

Microsystems Inc., Ontario, Canada) equipped with an ORCAflash 4.0 V.2 monochromatic camera (Hamamatsu Photonics, Bridgewater, NJ, USA). This experiment was done three times. The number of PLA dots per cell was quantified on 25 cells per condition for each experiment.

Measurement of PLD activity using IMPACT

For IMPACT, cells were seeded on a 24-well plate and protein expression was induced overnight with 1 µg/mL of tetracycline. Cells were pre-treated with FIPI (750 nM, 5282455MG, MilliporeSigma) or DMSO control for 30 min, followed by 3-azidopropanol (1 mM) (Yuan et al., 2012) and PMA (100nM, P8139, MilliporeSigma) for 30 min. Cells were washed 3 times with PBS and incubated with BCN-BODIPY (1 µM) (Alamudi et al., 2016) diluted in Tyrode's-HEPES buffer [135 mM NaCl, 5 mM KCl, 1.8 mM $CaCl_2$, 1 mM $MgCl_2$, 1mg/mL glucose, 1 mg/mL BSA, 20 mM HEPES, pH 7.4] for 30 min at 37 °C. Cells were rinsed twice with PBS and split into 3 wells of a 96-well v-bottom plate. The plate was centrifuged at 1000g for 2 min and cells were rinsed twice with PBS. Cells were fixed with 4% PFA in PBS followed by two additional PBS washes. Cells were resuspended in fluorescence-activated cell sorting (FACS) buffer [0.5% FBS in PBS] for FACS analysis, which was performed on a Thermo Fisher Attune NxT analyzer.

Statistical analyses

All quantification graphs were derived from Prism (GraphPad Software, v7.0a). Statistical significance was determined using Student t-tests or one-way analysis of variance (ANOVA), followed by Bonferroni's multiple comparison test where *, ** and *** represented $P < 0.05$, $P < 0.001$ and $P < 0.0001$ respectively. Sample sizes and number of replicates are mentioned in figure legends.

Online supplemental material

Fig. S1 shows the validation of the expression and biotinylation of ARF-BirA*-Flag cell lines. Fig. S2 shows the validation of the localization, expression and biotinylation of ARF-BirA*-Flag HeLa cells. Fig. S3 Shows a schematic representation of ARL4D and ARL10 GTPase features as compared to ARF1 and that ARL10 localisation to the mitochondria is independent of nucleotide-loaded status. Fig S4 shows the gene ontology analysis of biological processes enriched from the AP-MS on WT and mutant forms of ARL10-GFP with emphasis on TORC2 signaling and interaction with RICTOR. Fig S5 shows that ARL14 recruits the ESCPE-1 complex involved in CI-MPR retrograde trafficking. Table S1 provides a list of baits used for BioID experiments. Table S2 provides a list of antibodies used in this study. Table S3 provides a list of plasmids used in this study. Table S4 provides a list of siRNA sequences used in this study. Table S5 provides the list of oligonucleotides used in this study. Table S6 contains the AP-MS data.

DATA AVAILABILITY

The raw BioID proteomic data were deposited on MASSIVE for further exploration: https://doi.org/doi:10.25345/C50K26G6S. The complete lists of preys identified with their respective scores and annotations are also available online at the following website: http://prohits-web.lunenfeld.ca.

ACKNOWLEDGEMENT

The authors thank S. Taylor (University of Manchester, UK) for the gift of the Flp-In™ T-Rex™ HeLa cells. We also thank M.A. Frohman for the pCGN-HA-PLD1 plasmid. We recognize the technical assistance and expertise provided by the IRCM core facilities, including the proteomic facility, the microscopy facility (Dr. D. Filion) and the animal facility (S. Riverin). This work was supported by an operating grant from the Canadian Institutes of Health

Research to J.-F.C. and M.J.S. (PJT-178241). J.M.B. acknowledges support from the National Science Foundation (CAREER CHE-1749919), and S.H. acknowledges support from the National Institutes of Health (T32GM138826). M.J.S. holds a Canada Research Chair in Cancer Signaling and Structural Biology. L.Q. is a recipient of a Fonds de Recherche du Québec-Santé (FRQS) doctoral studentships. J.-F.C. holds the Canada Research Chair in Cancer Signaling and Metastasis and is supported by the Alain Fontaine Chair in Cancer Research from the IRCM Foundation. The authors declare no competing financial interests.

AUTHOR CONTRIBUTIONS

L.Q., A.R., J.B., J.M.B., M.J.S. and J.-F.C. designed the research. L.Q., A.R., J.B., S.H., Y.K., M.P.T. and D.F. performed the research. L.Q., A.R., J.B., S.H. analyzed the data. A.-C.G. and M.K. provided expertise and key reagents. L.Q., A.R. and J.-F.C. wrote the manuscript with inputs from all authors.

REFERENCES

Abou Jamra, R., O. Philippe, A. Raas-Rothschild, S.H. Eck, E. Graf, R. Buchert, G. Borck, A. Ekici, F.F. Brockschmidt, M.M. Nothen, A. Munnich, T.M. Strom, A. Reis, and L. Colleaux. 2011. Adaptor protein complex 4 deficiency causes severe autosomal-recessive intellectual disability, progressive spastic paraplegia, shy character, and short stature. *Am J Hum Genet*. 88:788-795.

Alamudi, S.H., R. Satapathy, J. Kim, D. Su, H. Ren, R. Das, L. Hu, E. Alvarado-Martinez, J.Y. Lee, C. Hoppmann, E. Pena-Cabrera, H.H. Ha, H.S. Park, L. Wang, and Y.T. Chang. 2016. Development of background-free tame fluorescent probes for intracellular live cell imaging. *Nat Commun*. 7:11964.

Amor, J.C., D.H. Harrison, R.A. Kahn, and D. Ringe. 1994. Structure of the human ADP-ribosylation factor 1 complexed with GDP. *Nature*. 372:704-708.

Antonny, B., S. Beraud-Dufour, P. Chardin, and M. Chabre. 1997. N-terminal hydrophobic residues of the G-protein ADP-ribosylation factor-1 insert into membrane phospholipids upon GDP to GTP exchange. *Biochemistry*. 36:4675-4684.

Assoum, M., C. Philippe, B. Isidor, L. Perrin, P. Makrythanasis, N. Sondheimer, C. Paris, J. Douglas, G. Lesca, S. Antonarakis, H. Hamamy, T. Jouan, Y. Duffourd, S. Auvin, A. Saunier, A. Begtrup, C. Nowak, N. Chatron, D. Ville, K. Mireskandari, P. Milani, P. Jonveaux, G. Lemeur, M. Milh, M. Amamoto, M. Kato, M. Nakashima, N. Miyake, N. Matsumoto, A. Masri, C. Thauvin-Robinet, J.B. Riviere, L. Faivre, and J. Thevenon. 2016. Autosomal-Recessive Mutations in AP3B2, Adaptor-Related Protein Complex 3 Beta 2 Subunit, Cause an Early-Onset Epileptic Encephalopathy with Optic Atrophy. *Am J Hum Genet*. 99:1368-1376.

Bagci, H., N. Sriskandarajah, A. Robert, J. Boulais, I.E. Elkholi, V. Tran, Z.Y. Lin, M.P. Thibault, N. Dube, D. Faubert, D.R. Hipfner, A.C. Gingras, and J.F. Cote. 2020. Mapping the proximity interaction network of the Rho-family GTPases reveals signalling pathways and regulatory mechanisms. *Nat Cell Biol*. 22:120-134.

Bhattarai, S.R., S. Begum, R. Popow, and E.J. Ezratty. 2019. The ciliary GTPase Arl3 maintains tissue architecture by directing planar spindle orientation during epidermal morphogenesis. *Development*. 146.

Bianchi, P., E. Fermo, C. Vercellati, C. Boschetti, W. Barcellini, A. Iurlo, A.P. Marcello, P.G. Righetti, and A. Zanella. 2009. Congenital dyserythropoietic anemia type II (CDAII) is caused by mutations in the SEC23B gene. *Hum Mutat*. 30:1292-1298.

Bonifacino, J.S., and J.H. Hurley. 2008. Retromer. *Curr Opin Cell Biol*. 20:427-436.

Bourne, H.R., D.A. Sanders, and F. McCormick. 1991. The GTPase superfamily: conserved structure and molecular mechanism. *Nature*. 349:117-127.

Boyadjiev, S.A., J.C. Fromme, J. Ben, S.S. Chong, C. Nauta, D.J. Hur, G. Zhang, S. Hamamoto, R. Schekman, M. Ravazzola, L. Orci, and W. Eyaid. 2006. Cranio-lenticulo-sutural dysplasia is caused by a SEC23A mutation leading to abnormal endoplasmic-reticulum-to-Golgi trafficking. *Nat Genet*. 38:1192-1197.

Bumpus, T.W., and J.M. Baskin. 2017. Clickable Substrate Mimics Enable Imaging of Phospholipase D Activity. *ACS Cent Sci*. 3:1070-1077.

Bumpus, T.W., D. Liang, and J.M. Baskin. 2020. IMPACT: Imaging phospholipase d activity with clickable alcohols via transphosphatidylation. *Methods Enzymol*. 641:75-94.

Casalou, C., A. Ferreira, and D.C. Barral. 2020. The Role of ARF Family Proteins and Their Regulators and Effectors in Cancer Progression: A Therapeutic Perspective. *Front Cell Dev Biol*. 8:217.

Chatr-Aryamontri, A., R. Oughtred, L. Boucher, J. Rust, C. Chang, N.K. Kolas, L. O'Donnell, S. Oster, C. Theesfeld, A. Sellam, C. Stark, B.J. Breitkreutz, K. Dolinski, and M. Tyers. 2017. The BioGRID interaction database: 2017 update. *Nucleic Acids Res*. 45:D369-D379.

Couzens, A.L., J.D. Knight, M.J. Kean, G. Teo, A. Weiss, W.H. Dunham, Z.Y. Lin, R.D. Bagshaw, F. Sicheri, T. Pawson, J.L. Wrana, H. Choi, and A.C. Gingras. 2013. Protein interaction network of the mammalian Hippo pathway reveals mechanisms of kinase-phosphatase interactions. *Sci Signal*. 6:rs15.

Craig, R., and R.C. Beavis. 2004. TANDEM: matching proteins with tandem mass spectra. *Bioinformatics*. 20:1466-1467.

D'Souza, R.S., R. Semus, E.A. Billings, C.B. Meyer, K. Conger, and J.E. Casanova. 2014. Rab4 orchestrates a small GTPase cascade for recruitment of adaptor proteins to early endosomes. *Curr Biol*. 24:1187-1198.

D'Souza-Schorey, C., and P. Chavrier. 2006. ARF proteins: roles in membrane traffic and beyond. *Nat Rev Mol Cell Biol*. 7:347-358.

Damseh, N., C.M. Danson, M. Al-Ashhab, B. Abu-Libdeh, M. Gallon, K. Sharma, B. Yaacov, E. Coulthard, M.A. Caldwell, S. Edvardson, P.J. Cullen, and O. Elpeleg. 2015. A defect in the retromer accessory protein, SNX27, manifests by infantile myoclonic epilepsy and neurodegeneration. *Neurogenetics*. 16:215-221.

Dewees, S.I., R. Vargova, K.R. Hardin, R.E. Turn, S. Devi, J. Linnert, U. Wolfrum, T. Caspary, M. Elias, and R.A. Kahn. 2022. Phylogenetic profiling and cellular analyses of ARL16 reveal roles in traffic of IFT140 and INPP5E. *Mol Biol Cell*. 33:ar33.

DiStasio, A., A. Driver, K. Sund, M. Donlin, R.M. Muraleedharan, S. Pooya, B. Kline-Fath, K.M. Kaufman, C.A. Prows, E. Schorry, B. Dasgupta, and R.W. Stottmann. 2017. Copb2 is essential for embryogenesis and hypomorphic mutations cause human microcephaly. *Hum Mol Genet*. 26:4836-4848.

Dittie, A.S., N. Hajibagheri, and S.A. Tooze. 1996. The AP-1 adaptor complex binds to immature secretory granules from PC12 cells, and is regulated by ADP-ribosylation factor. *J Cell Biol*. 132:523-536.

Ebner, M., B. Sinkovics, M. Szczygiel, D.W. Ribeiro, and I. Yudushkin. 2017. Localization of mTORC2 activity inside cells. *J Cell Biol*. 216:343-353.

Francis, J.W., D. Goswami, S.J. Novick, B.D. Pascal, E.R. Weikum, E.A. Ortlund, P.R. Griffin, and R.A. Kahn. 2017a. Nucleotide Binding to ARL2 in the TBCDARL2beta-Tubulin Complex Drives Conformational Changes in beta-Tubulin. *J Mol Biol*. 429:3696-3716.

Francis, J.W., L.E. Newman, L.A. Cunningham, and R.A. Kahn. 2017b. A Trimer Consisting of the Tubulin-specific Chaperone D (TBCD), Regulatory GTPase ARL2, and beta-Tubulin Is Required for Maintaining the Microtubule Network. *J Biol Chem*. 292:4336-4349.

Frohman, M.A., and A.J. Morris. 1999. Phospholipase D structure and regulation. *Chem Phys Lipids*. 98:127-140.

Garbes, L., K. Kim, A. Riess, H. Hoyer-Kuhn, F. Beleggia, A. Bevot, M.J. Kim, Y.H. Huh, H.S. Kweon, R. Savarirayan, D. Amor, P.M. Kakadia, T. Lindig, K.O. Kagan, J. Becker, S.A. Boyadjiev, B. Wollnik, O. Semler, S.K. Bohlander, J. Kim, and C. Netzer. 2015. Mutations in SEC24D, encoding a component of the COPII machinery, cause a syndromic form of osteogenesis imperfecta. *Am J Hum Genet*. 96:432-439.

Geers, B., J. Hagenstein, J. Endig, H. Ulrich, L. Fleig, P. Sprezyna, J. Mikulec, L. Heukamp, G. Tiegs, and L. Diehl. 2022. The ADP-Ribosylation Factor 4d Restricts Regulatory T-Cell Induction via Control of IL-2 Availability. *Cells*. 11.

Gillingham, A.K., and S. Munro. 2007. The small G proteins of the Arf family and their regulators. *Annu Rev Cell Dev Biol*. 23:579-611.

Go, C.D., J.D.R. Knight, A. Rajasekharan, B. Rathod, G.G. Hesketh, K.T. Abe, J.-Y. Youn, P. Samavarchi-Tehrani, H. Zhang, L.Y. Zhu, E. Popiel, J.-P. Lambert, É. Coyaud, S.W.T. Cheung, D. Rajendran, C.J. Wong, H. Antonicka, L. Pelletier, A.F. Palazzo, E.A.

Shoubridge, B. Raught, and A.-C. Gingras. 2021. A proximity-dependent biotinylation map of a human cell: an interactive web resource. *bioRxiv*.

Gotthardt, K., M. Lokaj, C. Koerner, N. Falk, A. Giessl, and A. Wittinghofer. 2015. A G-protein activation cascade from Arl13B to Arl3 and implications for ciliary targeting of lipidated proteins. *Elife*. 4.

Gu, Z., R. Eils, and M. Schlesner. 2016. Complex heatmaps reveal patterns and correlations in multidimensional genomic data. *Bioinformatics*. 32:2847-2849.

Guo, F., D. Yuan, J. Zhang, H. Zhang, C. Wang, L. Zhu, J. Zhang, Y. Pan, and C. Shao. 2019. Silencing of ARL14 Gene Induces Lung Adenocarcinoma Cells to a Dormant State. *Front Cell Dev Biol*. 7:238.

Gurumurthy, C.B., M. Sato, A. Nakamura, M. Inui, N. Kawano, M.A. Islam, S. Ogiwara, S. Takabayashi, M. Matsuyama, S. Nakagawa, H. Miura, and M. Ohtsuka. 2019. Creation of CRISPR-based germline-genome-engineered mice without ex vivo handling of zygotes by i-GONAD. *Nat Protoc*. 14:2452-2482.

Gustavsson, E.K., I. Guella, J. Trinh, C. Szu-Tu, A. Rajput, A.H. Rajput, J.C. Steele, M. McKeown, B.S. Jeon, J.O. Aasly, and M.J. Farrer. 2015. Genetic variability of the retromer cargo recognition complex in parkinsonism. *Mov Disord*. 30:580-584.

Hammond, S.M., Y.M. Altshuller, T.C. Sung, S.A. Rudge, K. Rose, J. Engebrecht, A.J. Morris, and M.A. Frohman. 1995. Human ADP-ribosylation factor-activated phosphatidylcholine-specific phospholipase D defines a new and highly conserved gene family. *J Biol Chem*. 270:29640-29643.

Hanzal-Bayer, M., M. Linari, and A. Wittinghofer. 2005. Properties of the interaction of Arf-like protein 2 with PDEdelta. *J Mol Biol*. 350:1074-1082.

Hirst, J., N.A. Bright, B. Rous, and M.S. Robinson. 1999. Characterization of a fourth adaptor-related protein complex. *Mol Biol Cell*. 10:2787-2802.

Hofmann, I., and S. Munro. 2006. An N-terminally acetylated Arf-like GTPase is localised to lysosomes and affects their motility. *J Cell Sci*. 119:1494-1503.

Honda, A., M. Nogami, T. Yokozeki, M. Yamazaki, H. Nakamura, H. Watanabe, K. Kawamoto, K. Nakayama, A.J. Morris, M.A. Frohman, and Y. Kanaho. 1999. Phosphatidylinositol 4-phosphate 5-kinase alpha is a downstream effector of the small G protein ARF6 in membrane ruffle formation. *Cell*. 99:521-532.

Izumi, K., M. Brett, E. Nishi, S. Drunat, E.S. Tan, K. Fujiki, S. Lebon, B. Cham, K. Masuda, M. Arakawa, A. Jacquinet, Y. Yamazumi, S.T. Chen, A. Verloes, Y. Okada, Y. Katou, T. Nakamura, T. Akiyama, P. Gressens, R. Foo, S. Passemard, E.C. Tan, V. El Ghouzzi, and

K. Shirahige. 2016. ARCN1 Mutations Cause a Recognizable Craniofacial Syndrome Due to COPI-Mediated Transport Defects. *Am J Hum Genet*. 99:451-459.

Jacobs, S., C. Schilf, F. Fliegert, S. Koling, Y. Weber, A. Schurmann, and H.G. Joost. 1999. ADP-ribosylation factor (ARF)-like 4, 6, and 7 represent a subgroup of the ARF family characterization by rapid nucleotide exchange and a nuclear localization signal. *FEBS Lett*. 456:384-388.

Jimenez, A., D. Chen, and N.M. Alto. 2016. How Bacteria Subvert Animal Cell Structure and Function. *Annu Rev Cell Dev Biol*. 32:373-397.

Jones, B., E.L. Jones, S.A. Bonney, H.N. Patel, A.R. Mensenkamp, S. Eichenbaum-Voline, M. Rudling, U. Myrdal, G. Annesi, S. Naik, N. Meadows, A. Quattrone, S.A. Islam, R.P. Naoumova, B. Angelin, R. Infante, E. Levy, C.C. Roy, P.S. Freemont, J. Scott, and C.C. Shoulders. 2003. Mutations in a Sar1 GTPase of COPII vesicles are associated with lipid absorption disorders. *Nat Genet*. 34:29-31.

Kahn, R.A., J. Cherfils, M. Elias, R.C. Lovering, S. Munro, and A. Schurmann. 2006. Nomenclature for the human Arf family of GTP-binding proteins: ARF, ARL, and SAR proteins. *J Cell Biol*. 172:645-650.

Kean, M.J., D.F. Ceccarelli, M. Goudreault, M. Sanches, S. Tate, B. Larsen, L.C. Gibson, W.B. Derry, I.C. Scott, L. Pelletier, G.S. Baillie, F. Sicheri, and A.C. Gingras. 2011. Structure-function analysis of core STRIPAK Proteins: a signaling complex implicated in Golgi polarization. *J Biol Chem*. 286:25065-25075.

Keller, A., A.I. Nesvizhskii, E. Kolker, and R. Aebersold. 2002. Empirical statistical model to estimate the accuracy of peptide identifications made by MS/MS and database search. *Anal Chem*. 74:5383-5392.

Kolberg, L., U. Raudvere, I. Kuzmin, J. Vilo, and H. Peterson. 2020. gprofiler2 -- an R package for gene list functional enrichment analysis and namespace conversion toolset g:Profiler. *F1000Res*. 9.

Kondo, Y., A. Hanai, W. Nakai, Y. Katoh, K. Nakayama, and H.W. Shin. 2012. ARF1 and ARF3 are required for the integrity of recycling endosomes and the recycling pathway. *Cell Struct Funct*. 37:141-154.

Konig, T., H. Nolte, M.J. Aaltonen, T. Tatsuta, M. Krols, T. Stroh, T. Langer, and H.M. McBride. 2021. MIROs and DRP1 drive mitochondrial-derived vesicle biogenesis and promote quality control. *Nat Cell Biol*. 23:1271-1286.

Kvainickas, A., A. Jimenez-Orgaz, H. Nagele, Z. Hu, J. Dengjel, and F. Steinberg. 2017. Cargo-selective SNX-BAR proteins mediate retromer trimer independent retrograde transport. *J Cell Biol*. 216:3677-3693.

Li, C.C., T.C. Chiang, T.S. Wu, G. Pacheco-Rodriguez, J. Moss, and F.J. Lee. 2007. ARL4D recruits cytohesin-2/ARNO to modulate actin remodeling. *Mol Biol Cell*. 18:4420-4437.

Li, F.L., Z. Wu, Y.Q. Gao, F.Z. Bowling, J.M. Franklin, C. Hu, R.T. Suhandynata, M.A. Frohman, M.V. Airola, H. Zhou, and K.L. Guan. 2022. Defining the proximal interaction networks of Arf GTPases reveals a mechanism for the regulation of PLD1 and PI4KB. *EMBO J*. 41:e110698.

Li, Y., Q. Wei, Y. Zhang, K. Ling, and J. Hu. 2010. The small GTPases ARL-13 and ARL-3 coordinate intraflagellar transport and ciliogenesis. *J Cell Biol*. 189:1039-1051.

Lin, S.J., C.F. Huang, T.S. Wu, C.C. Li, and F.S. Lee. 2020. Arl4D-EB1 interaction promotes centrosomal recruitment of EB1 and microtubule growth. *Mol Biol Cell*. 31:2348-2362.

Linari, M., M. Hanzal-Bayer, and J. Becker. 1999. The delta subunit of rod specific cyclic GMP phosphodiesterase, PDE delta, interacts with the Arf-like protein Arl3 in a GTP specific manner. *FEBS Lett*. 458:55-59.

Liu, G., J. Zhang, B. Larsen, C. Stark, A. Breitkreutz, Z.Y. Lin, B.J. Breitkreutz, Y. Ding, K. Colwill, A. Pasculescu, T. Pawson, J.L. Wrana, A.I. Nesvizhskii, B. Raught, M. Tyers, and A.C. Gingras. 2010. ProHits: integrated software for mass spectrometry-based interaction proteomics. *Nat Biotechnol*. 28:1015-1017.

Melville, D.B., S. Studer, and R. Schekman. 2020. Small sequence variations between two mammalian paralogs of the small GTPase SAR1 underlie functional differences in coat protein complex II assembly. *J Biol Chem*. 295:8401-8412.

Merico, D., R. Isserlin, O. Stueker, A. Emili, and G.D. Bader. 2010. Enrichment map: a network-based method for gene-set enrichment visualization and interpretation. *PLoS One*. 5:e13984.

Mirabelli, C., E.J. Sherman, J.B. Cunha, J.W. Wotring, J. El Saghir, J. Harder, M. Kretzler, J.Z. Sexton, B.T. Emmer, and C.E. Wobus. 2022. ARF6 is a host factor for SARS-CoV-2 infection in vitro. *bioRxiv*.

Montpetit, A., S. Cote, E. Brustein, C.A. Drouin, L. Lapointe, M. Boudreau, C. Meloche, R. Drouin, T.J. Hudson, P. Drapeau, and P. Cossette. 2008. Disruption of AP1S1, causing a novel neurocutaneous syndrome, perturbs development of the skin and spinal cord. *PLoS Genet*. 4:e1000296.

Mossessova, E., L.C. Bickford, and J. Goldberg. 2003. SNARE selectivity of the COPII coat. *Cell*. 114:483-495.

Nachury, M.V., A.V. Loktev, Q. Zhang, C.J. Westlake, J. Peranen, A. Merdes, D.C. Slusarski, R.H. Scheller, J.F. Bazan, V.C. Sheffield, and P.K. Jackson. 2007. A core complex of BBS proteins cooperates with the GTPase Rab8 to promote ciliary membrane biogenesis. *Cell*. 129:1201-1213.

Nacke, M., E. Sandilands, K. Nikolatou, A. Roman-Fernandez, S. Mason, R. Patel, S. Lilla, T. Yelland, L.C.A. Galbraith, E.C. Freckmann, L. McGarry, J.P. Morton, E. Shanks, H.Y. Leung, E. Markert, S. Ismail, S. Zanivan, K. Blyth, and D.M. Bryant. 2021. An ARF GTPase module promoting invasion and metastasis through regulating phosphoinositide metabolism. *Nat Commun*. 12:1623.

Nahle, S., L. Quirion, J. Boulais, H. Bagci, D. Faubert, A.C. Gingras, and J.F. Cote. 2022. Defining the interactomes of proteins involved in cytoskeletal dynamics using high-throughput proximity-dependent biotinylation in cellulo. *STAR Protoc*. 3:101075.

Nesbit, M.A., F.M. Hannan, S.A. Howles, A.A. Reed, T. Cranston, C.E. Thakker, L. Gregory, A.J. Rimmer, N. Rust, U. Graham, P.J. Morrison, S.J. Hunter, M.P. Whyte, G. McVean, D. Buck, and R.V. Thakker. 2013. Mutations in AP2S1 cause familial hypocalciuric hypercalcemia type 3. *Nat Genet*. 45:93-97.

Nesvizhskii, A.I., A. Keller, E. Kolker, and R. Aebersold. 2003. A statistical model for identifying proteins by tandem mass spectrometry. *Anal Chem*. 75:4646-4658.

Neuspiel, M., A.C. Schauss, E. Braschi, R. Zunino, P. Rippstein, R.A. Rachubinski, M.A. Andrade-Navarro, and H.M. McBride. 2008. Cargo-selected transport from the mitochondria to peroxisomes is mediated by vesicular carriers. *Curr Biol*. 18:102-108.

Newman, L.E., C.R. Schiavon, R.E. Turn, and R.A. Kahn. 2017. The ARL2 GTPase regulates mitochondrial fusion from the intermembrane space. *Cell Logist*. 7:e1340104.

Ooi, C.E., E.C. Dell'Angelica, and J.S. Bonifacino. 1998. ADP-Ribosylation factor 1 (ARF1) regulates recruitment of the AP-3 adaptor complex to membranes. *J Cell Biol*. 142:391-402.

Palmer, D.J., J.B. Helms, C.J. Beckers, L. Orci, and J.E. Rothman. 1993. Binding of coatomer to Golgi membranes requires ADP-ribosylation factor. *J Biol Chem*. 268:12083-12089.

Panic, B., O. Perisic, D.B. Veprintsev, R.L. Williams, and S. Munro. 2003. Structural basis for Arl1-dependent targeting of homodimeric GRIP domains to the Golgi apparatus. *Mol Cell*. 12:863-874.

Patel, M., T.C. Chiang, V. Tran, F.J. Lee, and J.F. Cote. 2011. The Arf family GTPase Arl4A complexes with ELMO proteins to promote actin cytoskeleton remodeling and reveals a versatile Ras-binding domain in the ELMO proteins family. *J Biol Chem*. 286:38969-38979.

Puertollano, R., P.A. Randazzo, J.F. Presley, L.M. Hartnell, and J.S. Bonifacino. 2001. The GGAs promote ARF-dependent recruitment of clathrin to the TGN. *Cell*. 105:93-102.

Raote, I., M. Chabanon, N. Walani, M. Arroyo, M.F. Garcia-Parajo, V. Malhotra, and F. Campelo. 2020. A physical mechanism of TANGO1-mediated bulky cargo export. *Elife*. 9.

Roth, M.G. 1999. Lipid regulators of membrane traffic through the Golgi complex. *Trends Cell Biol*. 9:174-179.

Roux, K.J., D.I. Kim, M. Raida, and B. Burke. 2012. A promiscuous biotin ligase fusion protein identifies proximal and interacting proteins in mammalian cells. *J Cell Biol*. 196:801-810.

Saito, K., M. Maeda, and T. Katada. 2017. Regulation of the Sar1 GTPase Cycle Is Necessary for Large Cargo Secretion from the Endoplasmic Reticulum. *Front Cell Dev Biol*. 5:75.

Saito, K., K. Yamashiro, Y. Ichikawa, P. Erlmann, K. Kontani, V. Malhotra, and T. Katada. 2011. cTAGE5 mediates collagen secretion through interaction with TANGO1 at endoplasmic reticulum exit sites. *Mol Biol Cell*. 22:2301-2308.

Sane, A., L. Ahmarani, E. Delvin, N. Auclair, S. Spahis, and E. Levy. 2019. SAR1B GTPase is necessary to protect intestinal cells from disorders of lipid homeostasis, oxidative stress, and inflammation. *J Lipid Res*. 60:1755-1764.

Santos, A.J., C. Nogueira, M. Ortega-Bellido, and V. Malhotra. 2016. TANGO1 and Mia2/cTAGE5 (TALI) cooperate to export bulky pre-chylomicrons/VLDLs from the endoplasmic reticulum. *J Cell Biol*. 213:343-354.

Santy, L.C., K.S. Ravichandran, and J.E. Casanova. 2005. The DOCK180/Elmo complex couples ARNO-mediated Arf6 activation to the downstream activation of Rac1. *Curr Biol*. 15:1749-1754.

Schindelin, J., I. Arganda-Carreras, E. Frise, V. Kaynig, M. Longair, T. Pietzsch, S. Preibisch, C. Rueden, S. Saalfeld, B. Schmid, J.Y. Tinevez, D.J. White, V. Hartenstein, K. Eliceiri, P. Tomancak, and A. Cardona. 2012. Fiji: an open-source platform for biological-image analysis. *Nat Methods*. 9:676-682.

Setty, S.R., M.E. Shin, A. Yoshino, M.S. Marks, and C.G. Burd. 2003. Golgi recruitment of GRIP domain proteins by Arf-like GTPase 1 is regulated by Arf-like GTPase 3. *Curr Biol*. 13:401-404.

Shannon, P., A. Markiel, O. Ozier, N.S. Baliga, J.T. Wang, D. Ramage, N. Amin, B. Schwikowski, and T. Ideker. 2003. Cytoscape: a software environment for integrated models of biomolecular interaction networks. *Genome Res*. 13:2498-2504.

Sheen, V.L., V.S. Ganesh, M. Topcu, G. Sebire, A. Bodell, R.S. Hill, P.E. Grant, Y.Y. Shugart, J. Imitola, S.J. Khoury, R. Guerrini, and C.A. Walsh. 2004. Mutations in ARFGEF2 implicate vesicle trafficking in neural progenitor proliferation and migration in the human cerebral cortex. *Nat Genet*. 36:69-76.

Shoulders, C.C., D.J. Stephens, and B. Jones. 2004. The intracellular transport of chylomicrons requires the small GTPase, Sar1b. *Curr Opin Lipidol*. 15:191-197.

Shteynberg, D., E.W. Deutsch, H. Lam, J.K. Eng, Z. Sun, N. Tasman, L. Mendoza, R.L. Moritz, R. Aebersold, and A.I. Nesvizhskii. 2011. iProphet: multi-level integrative analysis of shotgun proteomic data improves peptide and protein identification rates and error estimates. *Mol Cell Proteomics*. 10:M111 007690.

Simonetti, B., C.M. Danson, K.J. Heesom, and P.J. Cullen. 2017. Sequence-dependent cargo recognition by SNX-BARs mediates retromer-independent transport of CI-MPR. *J Cell Biol*. 216:3695-3712.

Simonetti, B., B. Paul, K. Chaudhari, S. Weeratunga, F. Steinberg, M. Gorla, K.J. Heesom, G.J. Bashaw, B.M. Collins, and P.J. Cullen. 2019. Molecular identification of a BAR domain-containing coat complex for endosomal recycling of transmembrane proteins. *Nat Cell Biol*. 21:1219-1233.

Slabicki, M., M. Theis, D.B. Krastev, S. Samsonov, E. Mundwiller, M. Junqueira, M. Paszkowski-Rogacz, J. Teyra, A.K. Heninger, I. Poser, F. Prieur, J. Truchetto, C. Confavreux, C. Marelli, A. Durr, J.P. Camdessanche, A. Brice, A. Shevchenko, M.T. Pisabarro, G. Stevanin, and F. Buchholz. 2010. A genome-scale DNA repair RNAi screen identifies SPG48 as a novel gene associated with hereditary spastic paraplegia. *PLoS Biol*. 8:e1000408.

Sowa, M.E., E.J. Bennett, S.P. Gygi, and J.W. Harper. 2009. Defining the human deubiquitinating enzyme interaction landscape. *Cell*. 138:389-403.

Stearns, T., M.C. Willingham, D. Botstein, and R.A. Kahn. 1990. ADP-ribosylation factor is functionally and physically associated with the Golgi complex. *Proc Natl Acad Sci U S A*. 87:1238-1242.

Sztul, E., P.W. Chen, J.E. Casanova, J. Cherfils, J.B. Dacks, D.G. Lambright, F.S. Lee, P.A. Randazzo, L.C. Santy, A. Schurmann, I. Wilhelmi, M.E. Yohe, and R.A. Kahn. 2019. ARF GTPases and their GEFs and GAPs: concepts and challenges. *Mol Biol Cell*. 30:1249-1271.

Tan, J.Z.A., and P.A. Gleeson. 2019. Cargo Sorting at the trans-Golgi Network for Shunting into Specific Transport Routes: Role of Arf Small G Proteins and Adaptor Complexes. *Cells*. 8.

Teo, G., G. Liu, J. Zhang, A.I. Nesvizhskii, A.C. Gingras, and H. Choi. 2014. SAINTexpress: improvements and additional features in Significance Analysis of INTeractome software. *J Proteomics*. 100:37-43.

Toda, K., M. Nogami, K. Murakami, Y. Kanaho, and K. Nakayama. 1999. Colocalization of phospholipase D1 and GTP-binding-defective mutant of ADP-ribosylation factor 6 to endosomes and lysosomes. *FEBS Lett*. 442:221-225.

Tolksdorf, F., J. Mikulec, B. Geers, J. Endig, P. Sprezyna, L.C. Heukamp, P.A. Knolle, W. Kolanus, and L. Diehl. 2018. The PDL1-inducible GTPase Arl4d controls T effector function by limiting IL-2 production. *Sci Rep*. 8:16123.

Uhlen, M., L. Fagerberg, B.M. Hallstrom, C. Lindskog, P. Oksvold, A. Mardinoglu, A. Sivertsson, C. Kampf, E. Sjostedt, A. Asplund, I. Olsson, K. Edlund, E. Lundberg, S. Navani, C.A. Szigyarto, J. Odeberg, D. Djureinovic, J.O. Takanen, S. Hober, T. Alm, P.H. Edqvist, H. Berling, H. Tegel, J. Mulder, J. Rockberg, P. Nilsson, J.M. Schwenk, M. Hamsten, K. von Feilitzen, M. Forsberg, L. Persson, F. Johansson, M. Zwahlen, G. von Heijne, J. Nielsen, and F. Ponten. 2015. Proteomics. Tissue-based map of the human proteome. *Science*. 347:1260419.

Veltel, S., R. Gasper, E. Eisenacher, and A. Wittinghofer. 2008. The retinitis pigmentosa 2 gene product is a GTPase-activating protein for Arf-like 3. *Nat Struct Mol Biol*. 15:373-380.

Volpicelli-Daley, L.A., Y. Li, C.J. Zhang, and R.A. Kahn. 2005. Isoform-selective effects of the depletion of ADP-ribosylation factors 1-5 on membrane traffic. *Mol Biol Cell*. 16:4495-4508.

Walther, D.M., and D. Rapaport. 2009. Biogenesis of mitochondrial outer membrane proteins. *Biochim Biophys Acta*. 1793:42-51.

Watkin, L.B., B. Jessen, W. Wiszniewski, T.J. Vece, M. Jan, Y. Sha, M. Thamsen, R.L. Santos-Cortez, K. Lee, T. Gambin, L.R. Forbes, C.S. Law, A. Stray-Pedersen, M.H. Cheng, E.M. Mace, M.S. Anderson, D. Liu, L.F. Tang, S.K. Nicholas, K. Nahmod, G. Makedonas, D.L. Canter, P.Y. Kwok, J. Hicks, K.D. Jones, S. Penney, S.N. Jhangiani, M.D. Rosenblum, S.D. Dell, M.R. Waterfield, F.R. Papa, D.M. Muzny, N. Zaitlen, S.M. Leal, C. Gonzaga-Jauregui, G. Baylor-Hopkins Center for Mendelian, E. Boerwinkle, N.T. Eissa, R.A. Gibbs, J.R. Lupski, J.S. Orange, and A.K. Shum. 2015. COPA mutations impair ER-Golgi transport and cause hereditary autoimmune-mediated lung disease and arthritis. *Nat Genet*. 47:654-660.

Yamauchi, J., Y. Miyamoto, T. Torii, R. Mizutani, K. Nakamura, A. Sanbe, H. Koide, S. Kusakawa, and A. Tanoue. 2009. Valproic acid-inducible Arl4D and cytohesin-2/ARNO, acting through the downstream Arf6, regulate neurite outgrowth in N1E-115 cells. *Exp Cell Res*. 315:2043-2052.

Yong, X., L. Zhao, W. Deng, H. Sun, X. Zhou, L. Mao, W. Hu, X. Shen, Q. Sun, D.D. Billadeau, Y. Xue, and D. Jia. 2020. Mechanism of cargo recognition by retromer-linked SNX-BAR proteins. *PLoS Biol*. 18:e3000631.

Yoshikawa, Y., T. Satoh, T. Tamura, P. Wei, S.E. Bilasy, H. Edamatsu, A. Aiba, K. Katagiri, T. Kinashi, K. Nakao, and T. Kataoka. 2007. The M-Ras-RA-GEF-2-Rap1 pathway mediates tumor necrosis factor-alpha dependent regulation of integrin activation in splenocytes. *Mol Biol Cell*. 18:2949-2959.

Yu, J., S.O. Ka, K.B. Kwon, S.M. Lee, J.W. Park, and B.H. Park. 2011. Overexpression of the small GTPase Arl4D suppresses adipogenesis. *Int J Mol Med*. 28:793-798.

Yuan, Z., G.C. Kuang, R.J. Clark, and L. Zhu. 2012. Chemoselective sequential "click" ligation using unsymmetrical bisazides. *Org Lett*. 14:2590-2593.

Zhang, B., A. Xu, D. Wu, W. Xia, P. Li, E. Wang, R. Han, P. Sun, S. Zhou, and R. Wang. 2021. ARL14 as a Prognostic Biomarker in Non-Small Cell Lung Cancer. *J Inflamm Res*. 14:6557-6574.

Zhou, C., L. Cunningham, A.I. Marcus, Y. Li, and R.A. Kahn. 2006. Arl2 and Arl3 regulate different microtubule-dependent processes. *Mol Biol Cell*. 17:2476-2487.

Zhou, Y.Q., K. Wang, X.Y. Wang, H.Y. Cui, Y. Zhao, P. Zhu, and Z.N. Chen. 2022. SARS-CoV-2 pseudovirus enters the host cells through spike protein-CD147 in an Arf6-dependent manner. *Emerg Microbes Infect*. 11:1135-1144.

Zhukovsky, M.A., A. Filograna, A. Luini, D. Corda, and C. Valente. 2019. Phosphatidic acid in membrane rearrangements. *FEBS Lett*. 593:2428-2451.

Zolotarov, Y., C. Ma, I. González-Recio, S. Hardy, G. Franken, N. Uetani, F. Latta, E. Kostantin, J. Boulais, M.-P. Thibault, J.-F. Côté, I.D. Moreno, A.D. Quintana, J.G.J. Hoenderop, L.A. Martínez-Cruz, M.L. Tremblay, and J.H.F. de Baaij. 2020. ARL15 modulates magnesium homeostasis through N-glycosylation of CNNMs. *bioRxiv*.

ABBREVIATIONS

ARF, ADP-ribosylation factor

ARL, ARF-like

ASS, ARF-specificity score

BioID, proximity-dependent biotin identification

CI-MPR, Cation-Independent Mannose-6-Phosphate Receptor

COPI, Coat Protein Complex I

COPII, Coat Protein Complex II

ER, endoplasmic reticulum

ERGIC, ER-Golgi intermediate compartment

ESCPE-1, endosomal SNX-BAR sorting complex for promoting exit 1

GEFs, guanine nucleotide exchange factors

GAPs, GTPase activating proteins

GO BP, Gene Ontology biological processes

PA, phosphatidic acid

PBR, polybasic region

PLA, proximity ligation assay

PLD1, phospholipase D1

TBCD, tubulin-specific chaperone D

TM, transmembrane

TOM20, mitochondrial import receptor subunit TOM20 homolog

TRIM23, tripartite motif-containing protein 23

FIGURE LEGENDS

Figure 1. The ARF proximity interaction network defined by BioID. (A) Pipeline of the ARF BioID method performed in Flp-In T-REx HEK293 and HeLa cell lines. The expression of the constitutively active bait fused to BirA*-Flag is induced with tetracycline for 24h in media supplemented with biotin allowing biotinylation of proximal proteins including effectors (χ) and GAPs (γ) (1). These proteins are then isolated (2) and purified by mass spectrometry (3). High confidence interactors were defined as those displaying an AvgP $\geq$ 0.95, a CAAX-ratio of over 1.7 and spectral counts of over 4.5 in HEK293 cells and 6 in HeLa cells. In HEK293 cells this corresponded to 1265 interactions and in Hela cells to 1671. The Venn diagram shows the number of interactions that are unique and shared between the two cell lines. **(B)** Proportional area chart representing the number of interactions identified for each bait (HEK293 in red and HeLa in light blue) and the overlap with the literature (dark blue) where everything is proportional to the total number of interactions in the two cell lines. The orange circle represents the interaction overlap between the HEK293 and HeLa cells. The numbers in light grey indicate the overlap percentage. The total overlap percentage between the two cells line and the total recall percentage are presented under the global column. **(C)** Known interactors of ARF GTPases involved in various cellular processes including COP mediated transport, cytoskeleton dynamics, glycosylation and trafficking were identified thereby validating the method. Interactors in lighter blue were present in our screen but did not pass our stringent thresholding. ER: endoplasmic reticulum.

Figure 2. ARF location assignment from BioID results. (A) Visual representation of the top 3 cell compartments enriched for each ARF assigned by Human Cell Map. The top 4 is represented when a tie is present in the analysis. **(B)** Dotplot representative of prey enriched for the top 3 cell compartments identified with Human Cell Map for constitutively active

ARF1, ARL4D and ARL10. **(C)** FlpIn T-REx HeLa cells expressing constitutively active ARL4D-BirA*-Flag transfected with POP1-YFP. ARL4D-BirA*-Flag was revealed with anti-Flag immunostaining and biotinylated proteins were revealed using Alexa Fluor 633-conjugated streptavidin. Blue arrowheads point to the nucleoli and n indicates the nucleus. Bar, 10 µm. **(D)** Co-immunostaining of FlpIn T-Rex Hela expressing wild-type ARL10-GFP using anti-TOM20 (mitochondria marker) and anti-PEX14 (peroxisomes marker). The enlargements show that ARL10 localizes predominantly at the mitochondria while high exposure of the same cell reveals the presence of ARL10 in peroxisomes. Images are representative of n=2 independent experiments. Bar, 10 µm. **(E)** Schematic representations of the ARL10 fragments used in this study. The light gray portion including the N-loop, the Switch1 (SW1) and Switch2 (SW2) represent the ARF homologue domain while the N-terminal region is represented in dark gray. The N-terminal region includes the putative TM domain represented in blue and is unique to ARL10. **(F)** Immunostaining of anti-TOM20 (mitochondria marker) and/or anti-GM130 (Golgi marker) was performed on FlpIn T-Rex Hela expressing the indicated GFP fusion to reveal translocation of GFP to these cell compartment by the addition of the indicated ARL10 fragments in N-terminal of the protein. Images are representative of n=2 independent experiments. Bar, 10µm. EE: early endosomes, ER: endoplasmic reticulum, ERGIC : ER-Golgi intermediate compartment, LE : late endosomes, PM: plasma membrane, RE: recycling endosomes.

Figure 3. Clusterization of ARFs candidate effectors. (A) Heatmap of the specificity of ARF potential effectors determined by the ASS score clustered with Peasron correlation. Dark purple indicates the strongest bait–prey specificity. **(B)** Zoom in of cluster 1, specific to constitutively active SAR1B. Proteins involved in the COPII machinery (light blue) and lipid biosynthesis (orange) are identified. **(C)** Zoom in of cluster 5 associated with constitutively active ARL4D

is shown at the top. The bottom represents an enrichment map of overrepresented GO biological processes performed using this specific cluster. Node size is representative of the number of proteins associated with each term and the length of the edges shows the interconnectivity between the terms. **(D)** Zoom in of cluster 2 and 3 associated with constitutively active ARL10 is shown at the top. The bottom represents an enrichment map of overrepresented GO biological processes performed using this specific cluster. The node sizes and edge lengths are defined as in C).

Figure 4. Mapping of ARF regulators. (A) and **(B)** Heatmap of the specificity ARF GAPs in (A) and ARF GEFs in (B) identified by BioID where dark purple indicates the strongest bait–prey specificity determined by the ASS score.

Figure 5. Characterization of ARL14, a PLD1 activator. (A) Schematic representation of murine *ARL14* coding region composed of only one exon used for genome editing where a 3x-Flag tag was added to the 3' end. The genotyping strategy is indicated with arrows representing the different primers. **(B)** Genotyping results of mice used for (C). Top represents amplification around the insertion site (primer 1 and 3) and bottom represents amplification in the insertion site (primer 1 and 2). **(C)** Western blot of organs from $ARL14^{+/+}$ (WT) or $ARL14^{+/3xFlag}$ knock-in mice at age P65. Coomassie staining was used to validate loading. **(D)** Graphical representation of preys identified in ARL14 BioID in FlpIn T-REx HEK293 and HeLa cells showing the normalized spectral counts (CBNP) on the X axis and the $\log_2$ fold change against the mean of the negative controls on the Y axis. **(E)** Dotplot showing BioID close proximity interactions of PLD1 with ARF GTPases in FlpIn T-REx HEK293 and HeLa cells. **(F)** PLA of FlpIn T-REx HeLa cells expressing ARL14 WT, constitutively active (Q68L) or nucleotide-free (S27N) for 16 hours tagged with GFP. Cells expressing GFP alone were used as a control.

F-actin staining (Alexa Fluor 568-Phalloidin) (not shown) was used to delineate the cell outline. Bar, 10 µm. **(G)** Quantification of (F) where the violin plot shows the number of PLA puncta per cell for each condition. Data are representative of n=3 independent experiments (total of 75 cells per condition). Statistics show the comparison of the GFP control to the ARL14 conditions. *P* values were calculated by one-way ANOVA followed by Bonferroni's test; ***$P < 0.0001$. **(H)** Quantification of PLD activity using IMPACT, where the graph shows the relative IMPACT fluorescence. The bar height represents the mean and error bars denote the standard deviation, n=3 independent experiments. Statistics above the graph are compared to the parental control. *P* values were calculated by one-way ANOVA, followed by Bonferroni's test; ***$P < 0.0001$, **$P<0.001$.

Figure 6. SNX1 is an effector of ARL14. (A) Dotplot showing BioID close proximity interactions of the ESCPE-1 complex with ARF GTPases in FlpIn T-REx HEK293 and HeLa cells. **(B)** PLA of FlpIn T-REx HeLa cells expressing ARL14 WT, constitutively active (Q68L) or nucleotide-free (S27N) for 16 hours tagged with GFP. Cells expressing GFP alone were used as a control. Bar, 10 µm. **(C)** Violin plot showing the quantification of the number of PLA puncta per cell for each condition. Data are representative of n=3 independent experiments (total of 90 cells per condition). *P* values compare the GFP control to the different ARL14 conditions and were calculated by one-way ANOVA followed by Bonferroni's test; ***$P< 0.0001$. **(D)** SNX1 immunostaining of FlpIn T-REx HeLa expressing ARL14-mScarlet WT, constitutively active (Q68L) or nucleotide-free (S27N). Enlargements show accumulation of SNX1-positive dots on ARL14-positive membranes for the WT or active form but not the nucleotide free form of ARL14. Bar, 10µm. **(E)** Violin plot showing the quantification of the relative mean fluorescence intensity (MFI) outside the TGN for each condition presented in (F). Data are representative of n=3 independent experiments (total of 90 cells per condition). *P*

values were calculated by by Student *t*-test; ***$P < 0.0001$; ***$P < 0.0001$. **(F)** Co-immunostainings using anti-Golgin97 as TGN marker and anti-CI-MPR in HeLa and ARL14 knock-out HeLa cells. Bar, 10µm.

Figure S1. Validation of the expression and biotinylation of ARF-BirA*-Flag cell lines. (A) and **(B)** Western blot of FlpIn T-REx HeLa cells expressing the indicated constitutively active ARF-BirA*-Flag construct treated for 24 hours with tetracycline and biotin. Loading controls are calnexin in (A) and GAPDH in (B). Data are representative of n=2 experiments. **(C)** and **(D)** Western blot of FlpIn T-REx HEK293 cells expressing the indicated constitutively active ARF-BirA*-Flag construct treated for 24 hours with tetracycline and biotin. Loading controls are GAPDH in (C) and calnexin in (D). Data are representative of n=2 experiments.

Figure S2. Validation of the localization, expression and biotinylation of ARF-BirA*-Flag HeLa cells. Confocal microscopy images of immunostaining against Flag (Alexa Fluor 488) and streptavidin (Alexa Fluor 647-Streptavidin) in FlpIn T-REx HeLa cells expressing the indicated constitutively active ARF-BirA*-Flag construct or control treated for 24 hours with tetracycline and biotin. Parental cells were used as control. When necessary, F-actin staining (Alexa Fluor 568-Phalloidin) (not shown) was used to delineate the cell outline. Bar, 10 µm. Data are representative of n=1 experiments.

Figure S3. ARL10 localization to the mitochondria is independent of nucleotide-loaded status. (A) Schematic representation of ARL4D and ARL10 GTPase features as compared to ARF1. Both ARL4D and ARL10 contain the core ARF GTPase region (in light grey) that includes the N-loop, Switch 1 (SW1) and switch 2 (SW2) regions that change conformation upon exchange of GDP for GTP. ARL4D contains a nuclear localization signal (NLS) in C-

terminus. The Myristoylated (Myr-) amphipathic helix that ensures tight membrane association of ARF1 is conserved in ARL4D but is replaced in ARL10 by a 76 amino acid sequence containing a predicted transmembrane (TM) domain enriched in hydrophobic residues followed by a stretch of positively charged (polybasic region, PBR) amino acids region. **(B)** Immunostaining of the mitochondria marker TOM20 in FlpIN T-Rex HeLa cells expressing ARL10-GFP, ARL10^{S132L}-GFP (constitutively active) or ARL10^{S91N}-GFP (nucleotide-free) shows that ARL10 localization to the mitochondria is independent from its nucleotide-loaded state.

Figure S4. ARL10 is involved in TORC2 signaling and interacts with RICTOR. (A) Overrepresentation analyses of GO biological processes enriched from the AP-MS of ARL10-GFP (WT), constitutively active (S132L) or nucleotide-free (S91N) in FlpIn T-REx HeLa cells. The intersection size represents the number of proteins associated with a biological process. **(B)** Dotplot showing AP-MS protein-protein interactions of the mTORC2 complex retrieved in ARL10-GFP (WT), constitutively active (S132L) or nucleotide-free (S91N) in FlpIn T-REx HeLa cells. **(C)** Co-immunoprecipitation of RICTOR by pulldown (PD) of ARL10-GFP WT, constitutively active or nucleotide-free using GFP selector affinity resin in FlpIn T-REx HeLa cells. The GFP targeted to mitochondria generated by fusion of ARL10$^{1-76}$ to GFP was used as control. Calnexin was used as loading control in the total cell lysate (TLC). Data are representative of n=3 experiments.

Figure S5. ARL14 recruits the ESCPE-1 complex involved in CI-MPR retrograde trafficking. (A) PLA of FlpIn T-REx HeLa cells expressing ARL14 WT, constitutively active (Q68L) or nucleotide-free (S27N) for 16 hours tagged with GFP. Cells expressing GFP alone were used as a control. Bar, 10 μm. Violin plot shows the quantification of the number of PLA

puncta per cell for each condition. Data are representative of n=3 independent experiments (total of 90 cells per condition). *P* values were calculated by one-way ANOVA followed by Bonferroni's test; ***$P < 0.0001$ and represent comparison with the GFP control. **(B)** SNX6 immunostaining of FlpIn T-REx HeLa expressing ARL14-mScarlet WT, constitutively active (Q68L) or nucleotide-free (S27N). Enlargements show the accumulation of SNX6-positive dots on ARL14-positive membranes for the WT or active form but not the nucleotide-free form of ARL14. Bar, 10 µm. **(C)** Schematic representation of CI-MPR trafficking. **(D)** Co-immunostainings using anti-Golgin97 as TGN marker and anti-CI-MPR of HeLa cells transfected with siCTRL or siSNX5 and siSNX6. Bar, 10µm. **(E)** Violin plot shows the quantification of the relative mean fluorescence intensity (MFI) outside the TGN for each condition. Data are representative of n=3 independent experiments (total of 90 cells per condition). *P* values were calculated by Student *t*-test; ***$P < 0.0001$. **(F)** Western blot showing SNX5 and SNX6 knock-down after 72h of treatment with the indicated siRNAs. Calnexin was used as loading control. Data are representative of n=3 independent experiments. **(G)** Sequencing results of the *ARL14* knock-out clone in HeLa cells. Sequences for the two gRNAs used are represented in bold and the STOP codons are identified in red. Hela cells have three copies of this region as shown by the three bands in the agarose gel. The highest band shows an insertion of a small sequence that led to a STOP codon addition. The middle band represents the generation of a single cut which shifted the reading frame and led to a STOP codon addition. The lowest band represents two cuts that led to the deletion of the region between gRNA 1 and 2.

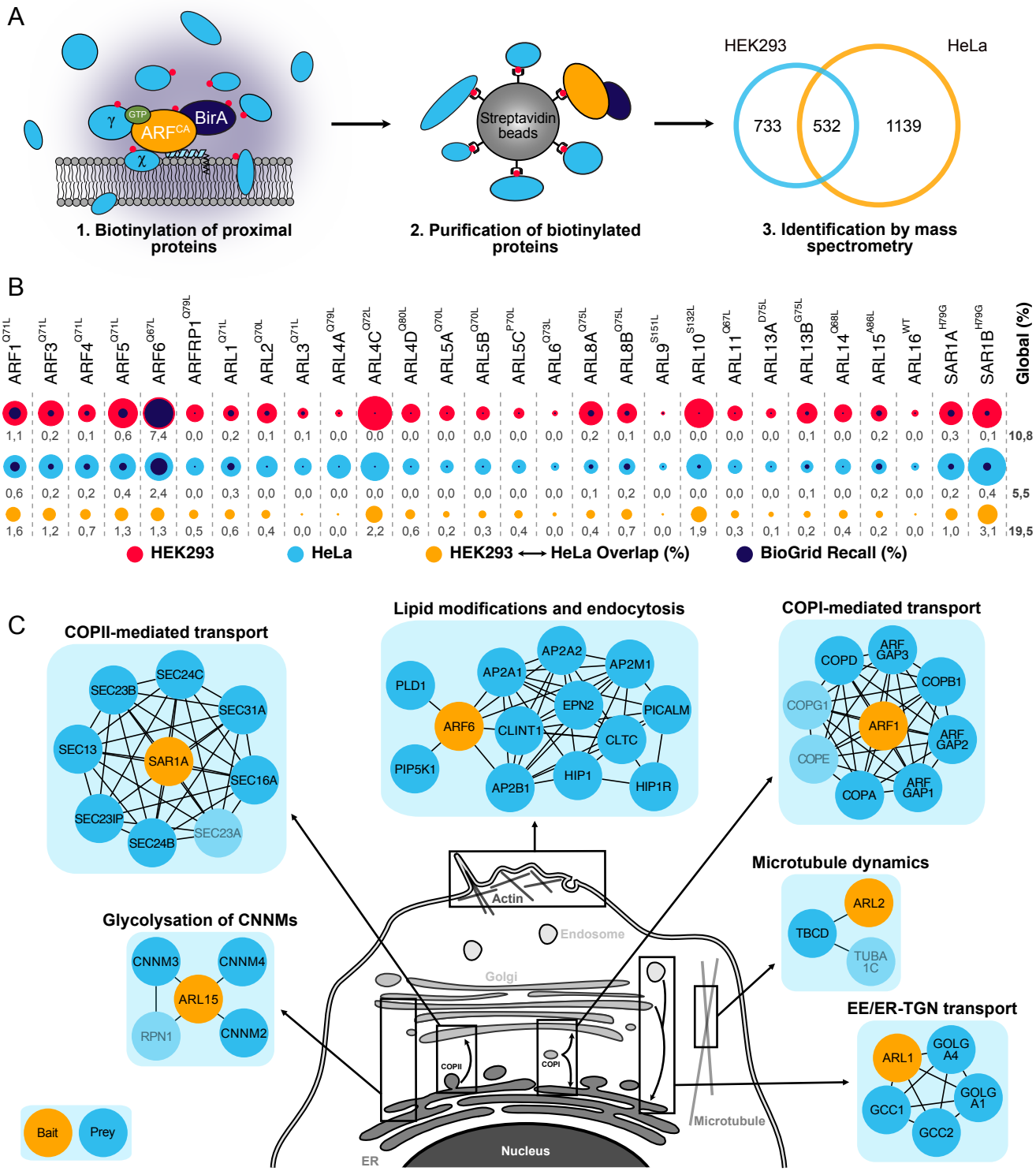
A
γ
GTP
ARF^CA
BirA
χ
1. Biotinylation of proximal proteins
Streptavidin beads
2. Purification of biotinylated proteins
HEK293
HeLa
733
532
1139
3. Identification by mass spectrometry
B
ARF1 Q71L
ARF3 Q71L
ARF4 Q71L
ARF5 Q71L
ARF6 Q67L
ARFRP1 Q79L
ARL1 Q71L
ARL2 Q70L
ARL3 Q71L
ARL4A Q79L
ARL4C Q72L
ARL4D Q80L
ARL5A Q70L
ARL5B Q70L
ARL5C P70L
ARL6 Q73L
ARL8A Q75L
ARL8B Q75L
ARL9 S151L
ARL10 S132L
ARL11 Q67L
ARL13A D75L
ARL13B G75L
ARL14 Q68L
ARL15 A86L
ARL16 WT
SAR1A H79G
SAR1B H79G
Global (%)
1,1 0,2 0,1 0,6 7,4 0,0 0,2 0,1 0,1 0,0 0,0 0,0 0,0 0,0 0,0 0,0 0,2 0,1 0,0 0,0 0,0 0,0 0,1 0,0 0,2 0,0 0,3 0,1 10,8
0,6 0,2 0,2 0,4 2,4 0,0 0,3 0,0 0,0 0,0 0,0 0,0 0,0 0,0 0,0 0,0 0,1 0,2 0,0 0,0 0,0 0,0 0,1 0,0 0,2 0,0 0,2 0,4 5,5
1,6 1,2 0,7 1,3 1,3 0,5 0,6 0,4 0,0 0,0 2,2 0,6 0,2 0,3 0,4 0,0 0,4 0,7 0,0 1,9 0,3 0,1 0,2 0,4 0,2 0,0 1,0 3,1 19,5
HEK293
HeLa
HEK293 ⟷ HeLa Overlap (%)
BioGrid Recall (%)
C
COPII-mediated transport
SEC24C
SEC23B
SEC31A
SEC13
SAR1A
SEC16A
SEC23IP
SEC24B
SEC23A
Lipid modifications and endocytosis
AP2A2
AP2A1
AP2M1
PLD1
EPN2
PICALM
ARF6
CLINT1
CLTC
PIP5K1
HIP1
AP2B1
HIP1R
COPI-mediated transport
COPD
ARF GAP3
COPB1
COPG1
ARF1
ARF GAP2
COPE
COPA
ARF GAP1
Microtubule dynamics
ARL2
TBCD
TUBA 1C
Glycolysation of CNNMs
CNNM3
CNNM4
ARL15
RPN1
CNNM2
EE/ER-TGN transport
ARL1
GOLG A4
GOLG A1
GCC1
GCC2
Actin
Endosome
Golgi
COPII
COPI
Microtubule
ER
Nucleus
Bait
Prey

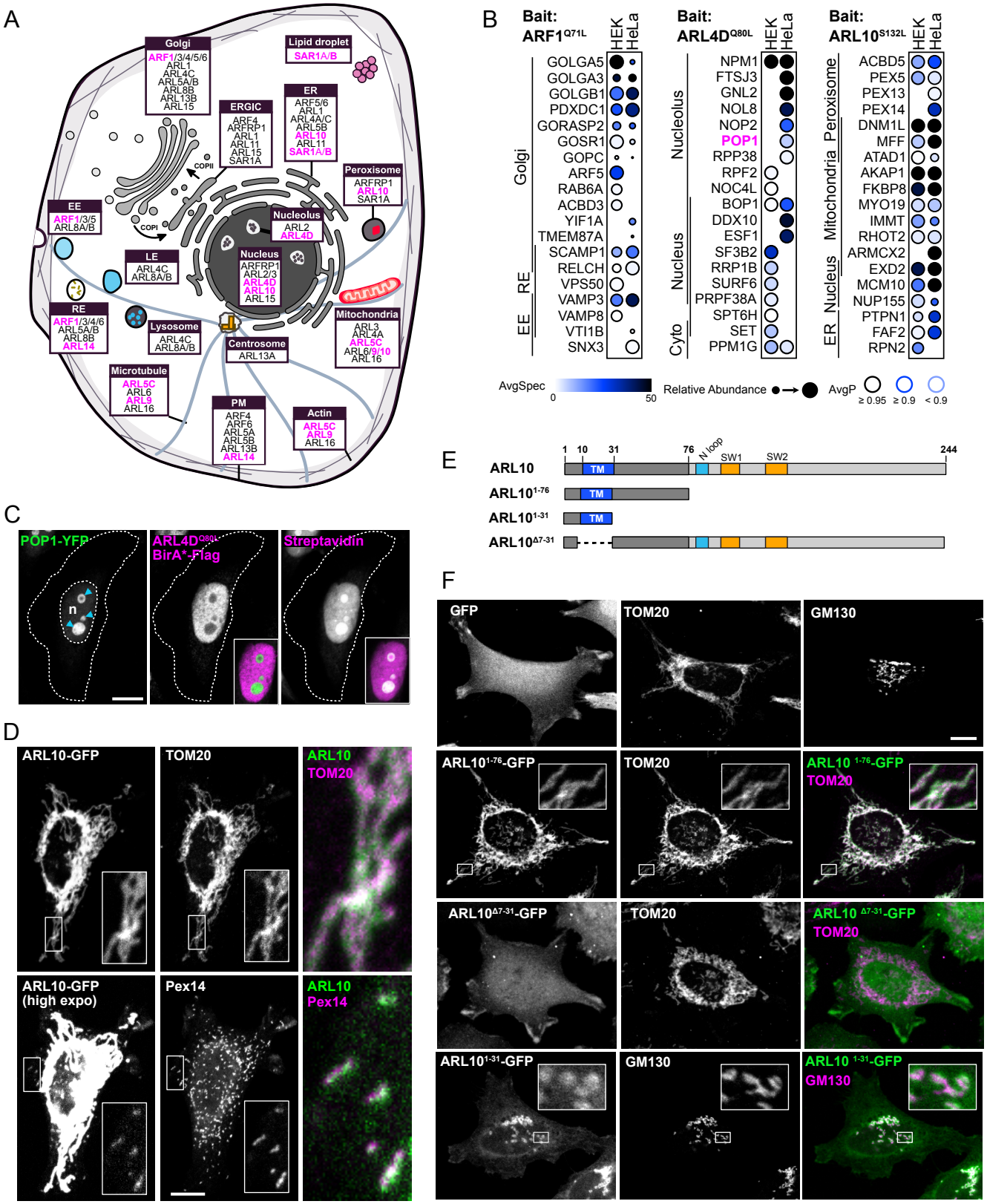
A
Golgi
ARF1/3/4/5/6
ARL1
ARL4C
ARL5A/B
ARL8B
ARL13B
ARL15
Lipid droplet
SAR1A/B
ER
ARF5/6
ARL1
ARL4A/C
ARL5B
ARL10
ARL11
SAR1A/B
ERGIC
ARF4
ARFRP1
ARL1
ARL11
ARL15
SAR1A
COPII
COPI
Peroxisome
ARFRP1
ARL10
SAR1A
EE
ARF1/3/5
ARL8A/B
Nucleolus
ARL2
ARL4D
LE
ARL4C
ARL8A/B
Nucleus
ARFRP1
ARL2/3
ARL4D
ARL10
ARL15
RE
ARF1/3/4/6
ARL5A/B
ARL8B
ARL14
Lysosome
ARL4C
ARL8A/B
Mitochondria
ARL3
ARL4A
ARL5C
ARL6/9/10
ARL16
Centrosome
ARL13A
Microtubule
ARL5C
ARL6
ARL9
ARL16
PM
ARF4
ARF6
ARL5A
ARL5B
ARL13B
ARL14
Actin
ARL5C
ARL9
ARL16
B
Bait:
ARF1Q71L
HEK
HeLa
Golgi
GOLGA5
GOLGA3
GOLGB1
PDXDC1
GORASP2
GOSR1
GOPC
ARF5
RAB6A
ACBD3
YIF1A
TMEM87A
RE
SCAMP1
RELCH
VPS50
VAMP3
EE
VAMP8
VTI1B
SNX3
Bait:
ARL4DQ80L
HEK
HeLa
Nucleolus
NPM1
FTSJ3
GNL2
NOL8
NOP2
POP1
RPP38
RPF2
NOC4L
BOP1
DDX10
ESF1
Nucleus
SF3B2
RRP1B
SURF6
PRPF38A
SPT6H
Cyto
SET
PPM1G
Bait:
ARL10S132L
HEK
HeLa
Peroxisome
ACBD5
PEX5
PEX13
PEX14
Mitochondria
DNM1L
MFF
ATAD1
AKAP1
FKBP8
MYO19
IMMT
RHOT2
Nucleus
ARMCX2
EXD2
MCM10
NUP155
ER
PTPN1
FAF2
RPN2
AvgSpec
0
50
Relative Abundance
AvgP
≥ 0.95
≥ 0.9
< 0.9
C
POP1-YFP
n
ARL4DQ80L
BirA*-Flag
Streptavidin
D
ARL10-GFP
TOM20
ARL10
TOM20
ARL10-GFP
(high expo)
Pex14
ARL10
Pex14
E
ARL10
1
10
31
76
N loop
SW1
SW2
244
TM
ARL10 1-76
ARL10 1-31
ARL10 Δ7-31
F
GFP
TOM20
GM130
ARL10 1-76-GFP
ARL10 1-76-GFP
TOM20
ARL10 Δ7-31-GFP
ARL10 Δ7-31-GFP
TOM20
ARL10 1-31-GFP
GM130
ARL10 1-31-GFP
GM130

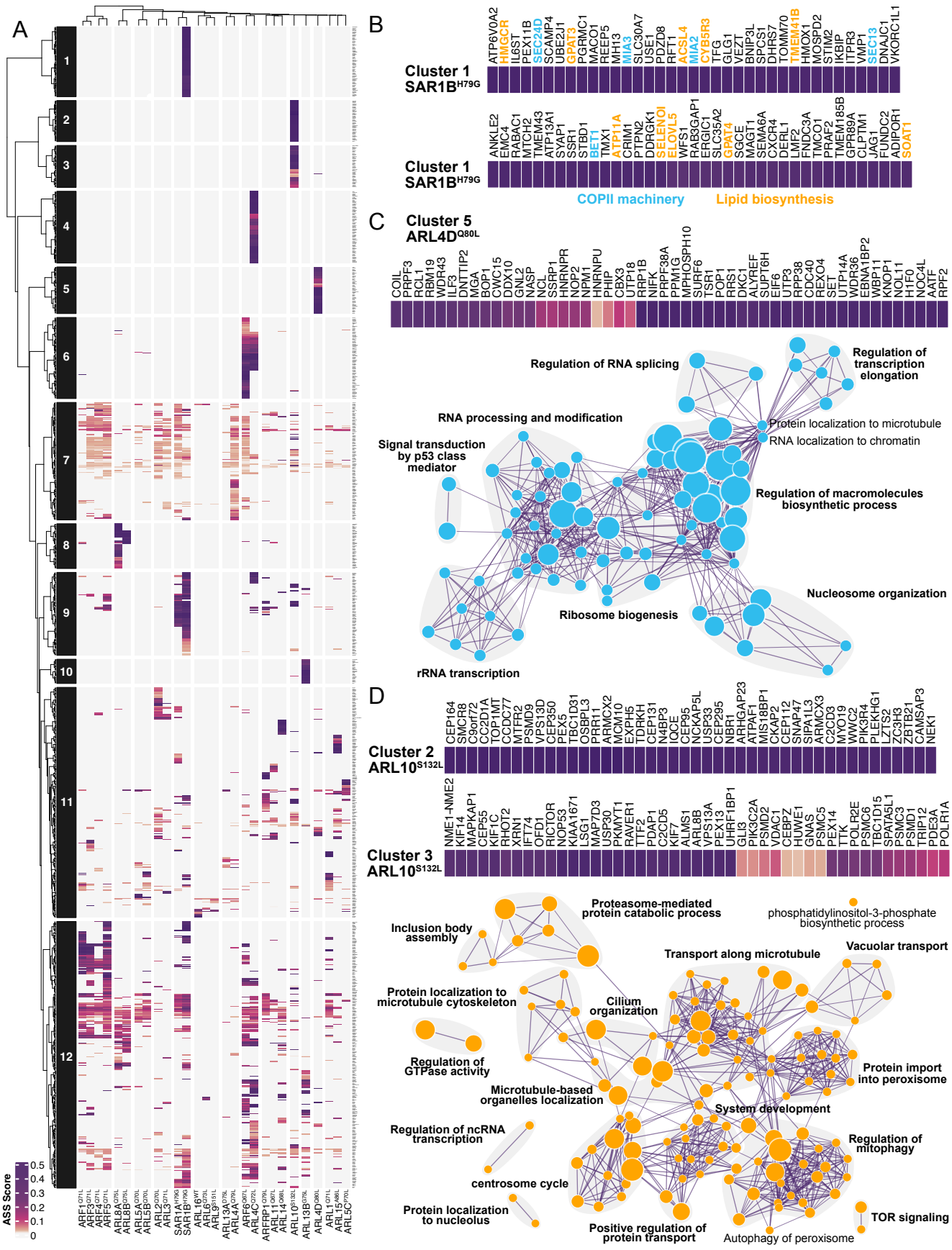
A
B
Cluster 1
SAR1B^{H79G}
ATP6V0A2 HMGCR IL6ST PEX11B SEC24D SCAMP4 UBE2J1 GPAT3 PGRMC1 MACO1 REEP5 MH13 MIA3 SLC30A7 USE1 PDZD8 RFT1 ACSL4 MIA2 CYB5R3 TFG GLG1 VEZT BNIP3L SPCS1 DHRS7 TOMM70 TMEM41B HMOX1 MOSPD2 STIM2 IKBIP ITPR3 VMP1 SEC13 DNAJC1 VKORC1L1
Cluster 1
SAR1B^{H79G}
ANKLE2 EMC4 RABAC1 MTCH2 TMEM43 ATP13A1 SYAP1 SSR1 STBD1 BET1 TMX1 ATP11A CRIM1 PTPN2 DDRGK1 SELENOI ELOVL5 WFS1 RAB3GAP1 ERGIC1 SLC35A2 GPAT4 SGCE MAGT1 SEMA6A CXCR4 DERL1 LMF2 FNDC3A TMCO1 PRAF2 TMEM185B GPR89A CLPTM1 JAG1 FUNDC2 ADIPOR1 SOAT1
COPII machinery
Lipid biosynthesis
C
Cluster 5
ARL4D^{Q80L}
COIL PRPF3 RCL1 RBM19 WDR43 ILF3 DNTTIP2 MGA BOP1 CWC15 DDX10 GNL2 NASP NCL SSRP1 HNRNPR NOP2 NPM1 HNRNPU PHIP CBX3 UTP18 RRP1B NIFK PRPF38A PPM1G MPHOSPH10 SURF6 TSR1 POP1 RRS1 DKC1 ALYREF SUPT6H EIF6 UTP3 RPP38 CDC40 REXO4 SET UTP14A WDR36 EBNA1BP2 WBP11 KNOP1 NOL11 H1F0 NOC4L AATF RPF2
Regulation of RNA splicing
Regulation of transcription elongation
RNA processing and modification
Protein localization to microtubule
RNA localization to chromatin
Signal transduction by p53 class mediator
Regulation of macromolecules biosynthetic process
Nucleosome organization
Ribosome biogenesis
rRNA transcription
D
Cluster 2
ARL10^{S132L}
CEP164 SMCR8 C9orf72 CC2D1A TOP1MT CCDC77 MTFR2 PSMD9 VPS13D CEP350 PEX5 TBC1D31 OSBPL3 PRR11 ARMCX2 MCM10 EXPH5 TDRKH CEP131 N4BP3 IQCE CEP95 NCKAP5L USP33 CEP295 NBR1 ARHGAP23 ATPAF1 MIS18BP1 CKAP2 CEP112 SNAP47 SIPA1L3 ARMCX3 C2CD3 MYO19 WWC2 PIK3R4 PLEKHG1 LZTS2 ZC3H3 ZBTB21 CAMSAP3 NEK1
Cluster 3
ARL10^{S132L}
NME1-NME2 KIF14 MAPKAP1 CEP55 KIF1C RHOT2 XRN1 IFT74 OFD1 RICTOR NOP53 KIAA1671 LSG1 MAP7D3 USP30 FKMYT1 RAVER1 TTF2 PDAP1 C2CD5 KIF7 ALMS1 ARL8B VPS13A PEX13 UHRF1BP1 GLI3 PIK3C2A PSMD2 VDAC1 CEBPZ HUWE1 GNAS PSMC5 PEX14 TTK POLR2E PSMC6 TBC1D15 SPATA5L1 PSMC3 PSMD1 TRIP12 PDE3A POLR1A
Proteasome-mediated protein catabolic process
phosphatidylinositol-3-phosphate biosynthetic process
Inclusion body assembly
Transport along microtubule
Vacuolar transport
Protein localization to microtubule cytoskeleton
Cilium organization
Regulation of GTPase activity
Protein import into peroxisome
Microtubule-based organelles localization
System development
Regulation of ncRNA transcription
Regulation of mitophagy
centrosome cycle
Protein localization to nucleolus
Positive regulation of protein transport
Autophagy of peroxisome
TOR signaling
ASS Score
0.5
0.4
0.3
0.2
0.1
0

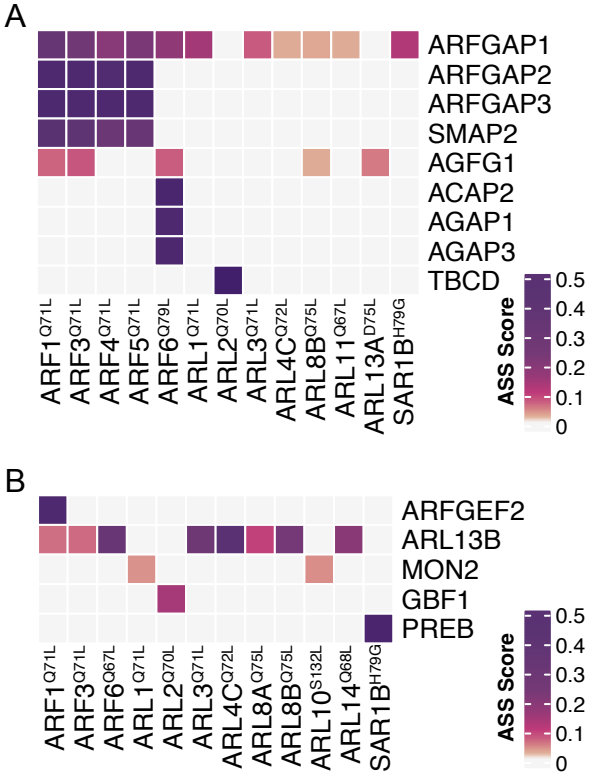
A
ARFGAP1
ARFGAP2
ARFGAP3
SMAP2
AGFG1
ACAP2
AGAP1
AGAP3
TBCD
ARF1Q71L
ARF3Q71L
ARF4Q71L
ARF5Q71L
ARF6Q79L
ARL1Q71L
ARL2Q70L
ARL3Q71L
ARL4CQ72L
ARL8BQ75L
ARL11Q67L
ARL13AD75L
SAR1BH79G
ASS Score
0.5
0.4
0.3
0.2
0.1
0
B
ARFGEF2
ARL13B
MON2
GBF1
PREB
ARF1Q71L
ARF3Q71L
ARF6Q67L
ARL1Q71L
ARL2Q70L
ARL3Q71L
ARL4CQ72L
ARL8AQ75L
ARL8BQ75L
ARL10S132L
ARL14Q68L
SAR1BH79G
ASS Score
0.5
0.4
0.3
0.2
0.1
0

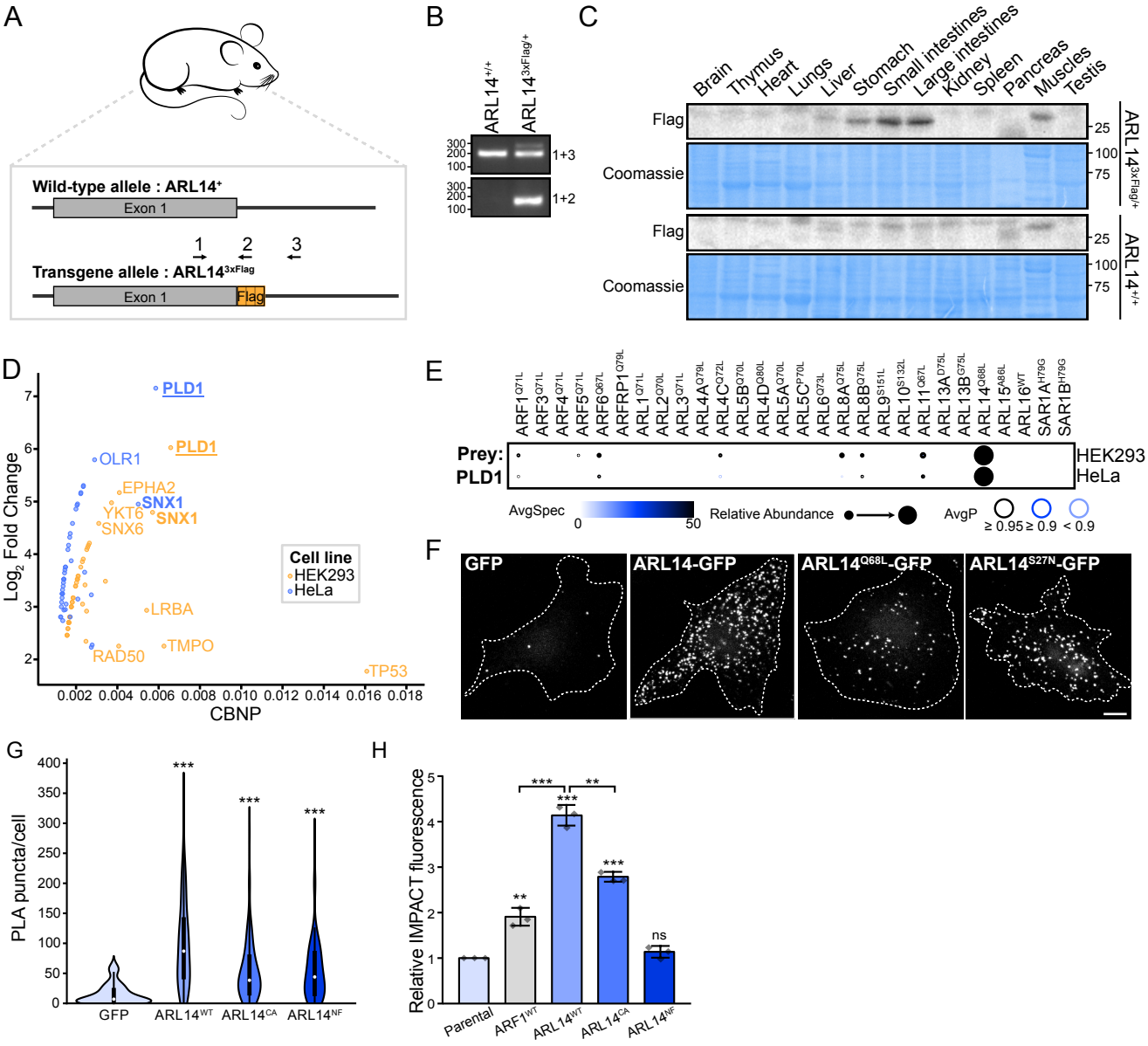
A
Wild-type allele : ARL14+
Exon 1
1
2
3
Transgene allele : ARL14 3xFlag
Exon 1
Flag
B
ARL14 +/+
ARL14 3xFlag/+
300
200
100
1+3
1+2
C
Brain
Thymus
Heart
Lungs
Liver
Stomach
Small intestines
Large intestines
Kidney
Spleen
Pancreas
Muscles
Testis
Flag
Coomassie
25
100
75
ARL14 3xFlag/+
ARL14 +/+
D
PLD1
PLD1
OLR1
EPHA2
SNX1
YKT6
SNX1
SNX6
LRBA
TMPO
RAD50
TP53
Cell line
HEK293
HeLa
Log2 Fold Change
CBNP
0.002 0.004 0.006 0.008 0.010 0.012 0.014 0.016 0.018
E
ARF1 Q71L
ARF3 Q71L
ARF4 Q71L
ARF5 Q71L
ARF6 Q67L
ARFRP1 Q79L
ARL1 Q71L
ARL2 Q70L
ARL3 Q71L
ARL4A Q79L
ARL4C Q72L
ARL5B Q70L
ARL4D Q80L
ARL5A Q70L
ARL5C P70L
ARL6 Q73L
ARL8A Q75L
ARL8B Q75L
ARL9 S151L
ARL10 S132L
ARL11 Q67L
ARL13A D75L
ARL13B G75L
ARL14 Q68L
ARL15 A86L
ARL16 WT
SAR1A H79G
SAR1B H79G
Prey:
PLD1
HEK293
HeLa
AvgSpec
0
50
Relative Abundance
AvgP
≥ 0.95
≥ 0.9
< 0.9
F
GFP
ARL14-GFP
ARL14 Q68L-GFP
ARL14 S27N-GFP
G
PLA puncta/cell
GFP
ARL14 WT
ARL14 CA
ARL14 NF
H
Relative IMPACT fluorescence
Parental
ARF1 WT
ARL14 WT
ARL14 CA
ARL14 NF
ns

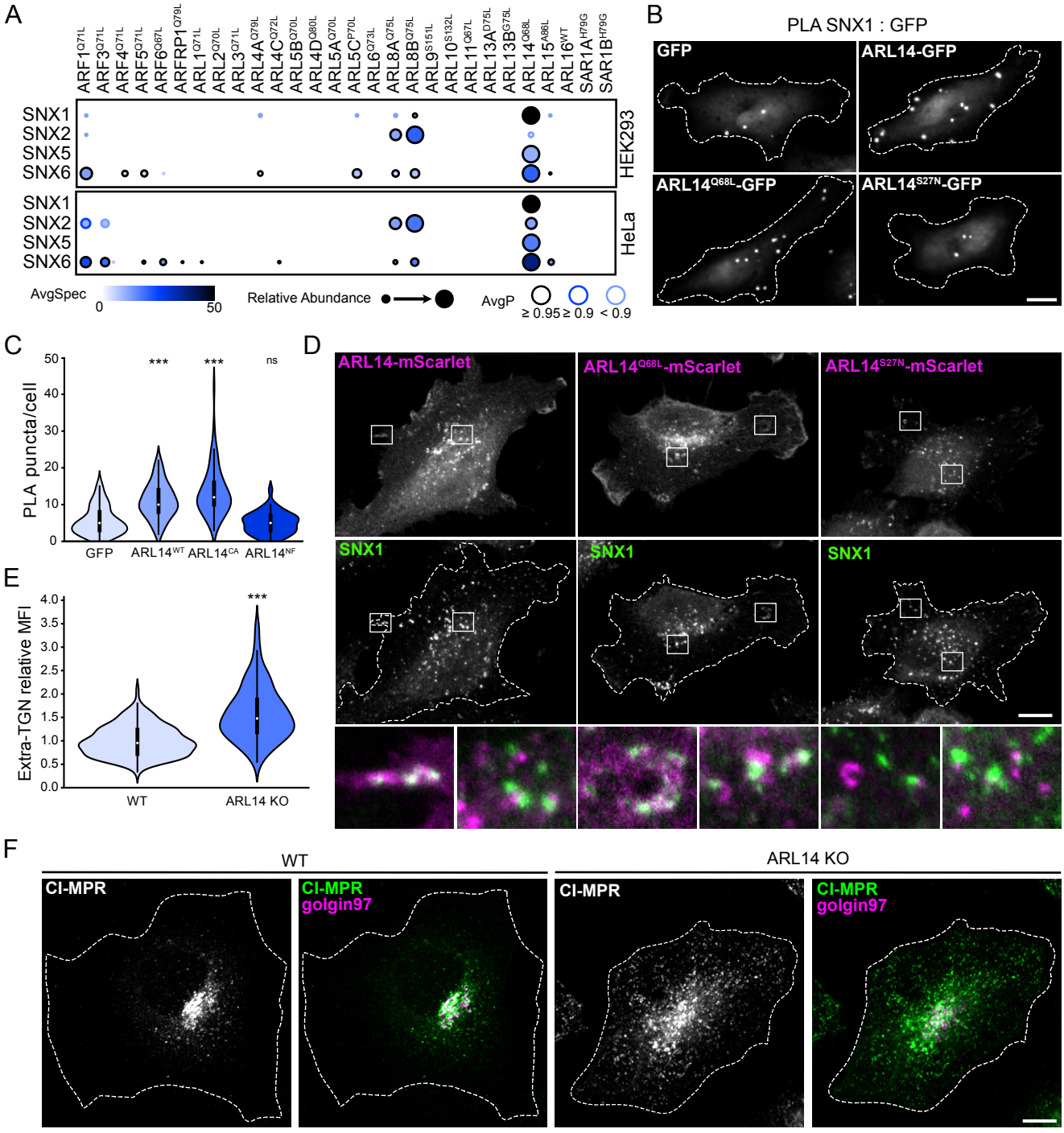
A
ARF1Q71L
ARF3Q71L
ARF4Q71L
ARF5Q71L
ARF6Q67L
ARFRP1Q79L
ARL1Q71L
ARL2Q70L
ARL3Q71L
ARL4AQ79L
ARL4CQ72L
ARL5BQ70L
ARL4DQ80L
ARL5AQ70L
ARL5CP70L
ARL6Q73L
ARL8AQ75L
ARL8BQ75L
ARL9S151L
ARL10S132L
ARL11Q67L
ARL13AD75L
ARL13BG75L
ARL14Q68L
ARL15A86L
ARL16WT
SAR1AH79G
SAR1BH79G
SNX1
SNX2
SNX5
SNX6
HEK293
HeLa
AvgSpec
0
50
Relative Abundance
AvgP
≥ 0.95
≥ 0.9
< 0.9
B
PLA SNX1 : GFP
GFP
ARL14-GFP
ARL14Q68L-GFP
ARL14S27N-GFP
C
PLA puncta/cell
***
***
ns
GFP
ARL14WT
ARL14CA
ARL14NF
D
ARL14-mScarlet
ARL14Q68L-mScarlet
ARL14S27N-mScarlet
SNX1
E
Extra-TGN relative MFI
***
WT
ARL14 KO
F
WT
ARL14 KO
CI-MPR
CI-MPR
golgin97